Linear and nonlinear evolution of the vertical shear instability in accretion discs

Richard P. Nelson^{1*}, Oliver Gressel^{1,2*} and Orkan M. Umurhan^{1,3*}

- ¹ Astronomy Unit, Queen Mary University of London, Mile End Road, London E1 4NS
- NORDITA, KTH Royal Institute of Technology and Stockholm University, Roslagstullsbacken 23, 106 91 Stockholm, Sweden
- ³ School of Natural Sciences, University of California, Merced, 5200 North Lake Rd, Merced, CA 95343, USA

Accepted 1988 December 15. Received 1988 December 14; in original form 1988 October 11

ABSTRACT

We analyse the stability and nonlinear dynamical evolution of power-law accretion disc models. These have midplane densities that follow radial power-laws, and have either temperature or entropy distributions that are strict power-law functions of cylindrical radius, R. We employ two different hydrodynamic codes to perform high resolution 2D-axisymmetric and 3D simulations that examine the long-term evolution of the disc models as a function of the power-law indices of the temperature or entropy, the thermal relaxation time of the fluid, and the disc viscosity. We present an accompanying stability analysis of the problem, based on asymptotic methods, that we use to interpret the results of the simulations. We find that axisymmetric disc models whose temperature or entropy profiles cause the equilibrium angular velocity to vary with height are unstable to the growth of modes with wavenumber ratios $|k_R/k_Z| \gg 1$ when the thermodynamic response of the fluid is isothermal, or the thermal evolution time is comparable to or shorter than the local dynamical time scale. These discs are subject to the Goldreich-Schubert-Fricke (GSF) or 'vertical shear' linear instability. Development of the instability involves excitation of vertical breathing and corrugation modes in the disc, with the corrugation modes in particular being a feature of the nonlinear saturated state. Instability is found to operate when the dimensionless disc kinematic viscosity $\nu < 10^{-6}$, corresponding to Reynolds numbers Re = $Hc_s/v > 2500$. In three dimensions the instability generates a quasiturbulent flow, and the associated Reynolds stress produces a fluctuating effective viscosity coefficient whose mean value reaches $\alpha \sim 6 \times 10^{-4}$ by the end of the simulation. The evolution and saturation of the vertical shear instability in astrophysical disc models which include realistic treatments of the thermal physics has yet to be examined. Should it occur on either global or local scales, however, our results suggest that it will have significant consequences for their internal dynamics, transport properties, and observational appearance.

Key words: accretion discs – instabilities – methods: numerical,analytical – planetary systems: protoplanetary disks

1 INTRODUCTION

Accretion discs play important roles in a broad range of astrophysical phenomena. Protostellar discs orbiting young stars provide conduits through which most of the mass accretes during the star formation process, and they are the nascent environments for planetary system formation. Mass transfer through Roche lobe overflow in close binary systems leads to highly energetic and time variable phenomena because of accretion through a disc onto compact objects such as white dwarfs in cataclysmic variables, and neutron stars or black holes in low mass X-ray binaries. Quasars and active galactic nuclei are powered by disc accretion onto supermassive

* E-mail: r.p.nelson@qmul.ac.uk (RPN); o.gressel@qmul.ac.uk (OG); oumurhan@ucmerced.edu (OMU)

black holes. Understanding the dynamics and evolution of astrophysical discs is key to understanding these and related phenomena.

Since the early work of Shakura & Sunyaev (1973) and Lynden-Bell & Pringle (1974), significant efforts have been made to understand the internal dynamics of discs, including mechanism(s) that allow them to transport angular momentum and accrete at their observed rates. Several ideas based on dynamical instabilities in non-magnetised flows have been explored, including the Papaloizou-Pringle instability for thick accretion tori driven by unstable non-axisymmetric wave modes (Papaloizou & Pringle 1984), convective instability (Cameron & Pine 1973; Lin & Papaloizou 1980; Ruden et al. 1988; Ryu & Goodman 1992), gravitational instability (Toomre 1964; Lin & Pringle 1987; Papaloizou & Savonije 1991), the global and subcritical baroclinic instabilities

2 Nelson, Gressel & Umurhan

(Klahr & Bodenheimer 2003; Johnson & Gammie 2006; Petersen et al. 2007; Lesur & Papaloizou 2010), and the vertical shear instability (Urpin & Brandenburg 1998; Urpin 2003; Arlt & Urpin 2004) which is closely related to the Goldreich-Schubert-Fricke (GSF) instability (Goldreich & Schubert 1967; Fricke 1968) developed in the context of differentially rotating stars. The presence of a weak magnetic field in the disc, however, leads to the development of magnetohydrodynamic turbulence driven by the magnetorotational instability (Balbus & Hawley 1991; Hawley & Balbus 1991), and it is now generally accepted that this is likely to be the source of anomalous viscosity in most accretion discs in which the magnetic field is well-coupled to the gas.

In this paper we present an extensive analysis of the hydrodynamic stability and nonlinear dynamics of disc models with powerlaw midplane density distributions, and either temperature or entropy profiles that are power-law function of R only, where R is the cylindrical radius. Our investigation employs high resolution 2Daxisymmetric and 3D hydrodynamic simulations and a linear stability analysis based on asymptotic methods. Models with powerlaw temperature profiles, adopting locally isothermal equations of state, have been used extensively in the study of protostellar disc dynamics and disc planet interactions. These studies normally assume the disc is viscous (e.g. Kley et al. 2001; Cresswell et al. 2007; Fragner & Nelson 2010; D'Angelo & Lubow 2010), or magnetised (e.g. Fromang & Nelson 2006; Beckwith et al. 2011), but in this study we include neither viscosity nor magnetic fields. Adoption of radial variations in temperature or entropy in the models causes them to have angular velocity profiles that are a function of both radius and height, $\Omega(R, Z)$. The height-variation of Ω is often referred to as the thermal wind in studies of atmospheric dynamics.

We find that disc models for which $d\Omega/dZ \neq 0$, and which experience thermal relaxation on ~ dynamical time scales or shorter, are unstable to the growth of modes with $|k_R/k_Z| \gg 1$, where (k_R, k_Z) are the radial and vertical wavenumbers. This instability appears to be closely related to the GSF instability, as studied by Urpin & Brandenburg (1998), Urpin (2003) and Arlt & Urpin (2004) in the context of accretion discs, and confirmed by our own linear stability analysis. Growth of the instability is favoured when the thermodynamic response of the gas is isothermal, of near-isothermal, although the strength of this dependence varies with model parameters with steeper thermal gradients displaying a greater tendency toward instability. The one 3D simulation we presents suggests that nonlinear development of the instability leads to a turbulent flow whose associated Reynolds stress leads to an effective alpha parameter $\alpha \sim 10^{-3}$, causing non-negligible outward angular momentum transport.

This paper is organised as follows. In Sect. 2 we present the basic equations of the problem, and the disc models we examine. In Sect. 3 we discuss the hydrodynamic stability of rotating shear flows, and previous work in the literature relevant to the present study. In Sect. 4 we describe the numerical methods employed, and in Sect. 5 we present the results of the nonlinear simulations. A stability analysis of the problem using asymptotic methods is presented in Sect. 6, and a reworking of the analysis of Goldreich & Schubert (1967) for a fully compressible fluid is given in the appendix. We draw our conclusions and discuss ideas for future work in Sect. 7.

2 BASIC EQUATIONS

In this paper we make use of both cylindrical polar coordinates (R, ϕ, Z) and spherical polar coordinates (r, θ, ϕ) . We solve the continuity, momentum and internal energy equations of hydrodynamics

$$\partial_{t}\rho + \nabla \cdot (\rho \mathbf{v}) = 0,
\partial_{t}(\rho \mathbf{v}) + \nabla \cdot [\rho \mathbf{v}\mathbf{v}] = -\nabla P - \nabla \Phi,
\partial_{t}(e) + \nabla \cdot (e\mathbf{v}) = -P\nabla \cdot \mathbf{v} + S - Q$$
(1)

where ρ is the density, \mathbf{v} is the velocity, P is is the pressure, e is the internal energy per unit volume, S and Q are energy source and sink terms, and $\Phi = -GM/r$ is the gravitational potential due to the central star. Here G is the gravitational constant and M is the mass of the star.

2.1 Disc models

We are concerned primarily with two basic equilibrium disc models in this paper. In the first, the temperature, T, and midplane density, $\rho_{\rm mid}$, are simple power-law functions of cylindrical radius:

$$T(R) = T_0 \left(\frac{R}{R_0}\right)^q \tag{2}$$

$$\rho_{\text{mid}}(R) = \rho_0 \left(\frac{R}{R_0}\right)^p, \tag{3}$$

where T_0 is the temperature at the fiducial radius R_0 , and ρ_0 is the midplane gas density there. Adopting an ideal gas equation of state

$$P = \frac{\mathcal{R}}{\mu} T \rho,\tag{4}$$

where \mathcal{R} is the gas constant and μ is the mean molecular weight, we note that the isothermal sound speed is related to the temperature through the expression $c_s^2 = \mathcal{R}T/\mu$, such that q also represents the radial power-law dependence of $c_s^2(R)$:

$$c_s^2(R) = c_0^2 \left(\frac{R}{R_0}\right)^q. {5}$$

In the second disc model, we adopt a power-law function for the midplane density, as in eqn. (3), and specify the entropy function, K_s , as a strict power-law function of R in the initial model:

$$K_s(R) = K_0 \left(\frac{R}{R_0}\right)^s,\tag{6}$$

where the entropy function is defined through the expression

$$P = K_s \rho^{\gamma},\tag{7}$$

and γ is assumed to be constant. The entropy per unit mass is given by

$$S = c_{v} \log \left(T \rho^{1-\gamma} \right) \tag{8}$$

where c_v is the specific heat at constant volume, and the entropy function is given in terms of the entropy by the expression

$$K_s = c_v(\gamma - 1) \exp\left(\frac{S}{c_v}\right). \tag{9}$$

2.1.1 Equilibrium solutions

In order to construct initial conditions for our simulations we need to obtain equilibrium disc models. The equations of force balance in the radial and vertical directions are given by

$$R\Omega^2 - \frac{GMR}{(R^2 + Z^2)^{3/2}} - \frac{1}{\rho} \frac{\partial P}{\partial R} = 0$$
 (10)

$$-\frac{GMZ}{(R^2+Z^2)^{3/2}} - \frac{1}{\rho} \frac{\partial P}{\partial Z} = 0. \tag{11}$$

Combining eqns. (10), (11), (2) and (3) leads to expressions for the equilibrium density and angular velocity, Ω , as functions of (R, Z) for the disc with a power-law temperature profile:

$$\rho(R,Z) = \rho_0 \left(\frac{R}{R_0}\right)^p \exp\left(\frac{GM}{c_s^2} \left[\frac{1}{\sqrt{R^2 + Z^2}} - \frac{1}{R}\right]\right), \tag{12}$$

$$\Omega(R,Z) = \Omega_K \left[(p+q) \left(\frac{H}{R} \right)^2 + (1+q) - \frac{qR}{\sqrt{R^2 + Z^2}} \right]^{1/2}$$
 (13)

where $\Omega_K = \sqrt{GM/R^3}$ is the keplerian angular velocity at radius R, and $H = c_s/\Omega_K$ is the local disc scale height (also see Takeuchi & Lin 2002; Fromang et al. 2011a). The definition of c_s given in eqn. (5) implies that

$$H = H_0 \left(\frac{R}{R_0}\right)^{(q+3)/2} \tag{14}$$

where $H_0 = c_0 / \sqrt{GM/R_0^3}$ is the disc scale height at radius R_0 .

Similarly, the equilibrium density and angular velocity for the disc model with a power-law entropy function profile are given by:

$$\rho(R,Z) = \left(\rho_{\text{mid}}^{(\gamma-1)} + \frac{(\gamma-1)}{\gamma} \frac{GM}{K_s} \left[\frac{1}{\sqrt{R^2 + Z^2}} - \frac{1}{R} \right]^{1/(\gamma-1)}$$
(15)

$$\Omega(R,Z) = \Omega_K \left[\frac{p}{\mathcal{M}_{\text{mid}}^2} + \frac{s}{\gamma \mathcal{M}^2} + (1+s) - \frac{sR}{\sqrt{R^2 + Z^2}} \right]^{1/2}, \quad (16)$$

where $\mathcal{M}_{\text{mid}} = v_K/a_{\text{mid}}$ is the Mach number at the disc midplane and $\mathcal{M} = v_K/a_s$ is the Mach number at each disc location. $v_K = \sqrt{GM/R}$ is the keplerian velocity at radius R, and the adiabatic sound speed $a_s = \sqrt{\gamma P/\rho}$, which takes the value a_{mid} at the disc midplane. We note that combining equations (4), (6), (7) and (15) demonstrates that the temperature in this model is a function of both R and Z in general:

$$T(R,Z) = K_s \rho^{\gamma - 1} \frac{\mu}{\mathcal{R}}.$$
 (17)

As such, this model provides a useful contrast to the one with temperature constant on cylinders, and is convenient to implement numerically because of the existence of analytic solutions for the equilibrium $\rho(R,Z)$ and $\Omega(R,Z)$ profiles.

Equations (2), (3), (12) and (13) fully specify the initial disc models with power-law temperature profiles that we examine in this paper, subject to appropriate choices for p and q. The expressions (3) and (6), along with (15) and (16), specify the initial models for which the entropy function is a power-law function of cylindrical radius, subject again to appropriate choices for the power-law exponents p and s. We note that for all models in which the initial temperature, T, or entropy function, K_s , are strict power-law functions of R, the equilibirum angular velocities are explicit functions of both R and Z, a fact that appears to play a key role in the disc instability that we examine in this paper. The dependence of Ω on Z is often referred to as the 'thermal wind' in studies of planetary atmosphere dynamics.

2.2 Thermodynamic evolution

The thermodynamic evolution of both disc models described above in Sect. 2.1 is assumed to be one of three types in the simulations

presented here: *locally isothermal*, for which the local temperature at each (R, Z) position in the disc is kept strictly equal to its original value; *isentropic*, where the entropy of the fluid is kept constant (equivalent to there being no source/sink term in the energy eqn. [1]); *thermally relaxing*, where we relax the temperature at each location in the disc toward its initial value on some time scale, $\tau_{\rm relax}$. The thermal relaxation model we adopt is

$$\frac{\mathrm{d}T}{\mathrm{d}t} = -\frac{(T - T_0)}{\tau_{\mathrm{relax}}} \tag{18}$$

where T_0 is the initial temperature. For simplicity, we assume that $\tau_{\rm relax}$ is a function of R, being a fixed multiple or fraction of the local keplerian orbital period. Equation (18) has a simple analytic solution of the form

$$T(t + \Delta t) = T_0 + (T(t) - T_0) \exp\left(-\frac{\Delta t}{\tau_{\text{relax}}}\right),\tag{19}$$

where T(t) is the temperature at time t, and $T(t + \Delta t)$ is the temperature at some later time $t + \Delta t$.

In the locally isothermal models we use an isothermal equation of state $P = c_s^2 \rho$, and do not evolve the energy equation in eqn. (1). In the isentropic models we use the equation of state $P = (\gamma - 1)e$, solve the energy equation in eqn. (1), and neglect the source and sink terms. The energy equation is also solved in the thermally relaxing models, along with eqn. (18) which plays the role of the source and sink terms in the energy equation (1).

3 HYDRODYNAMIC STABILITY OF DISC MODELS

3.1 The Rayleigh and Solberg-Høiland criteria

The Rayleigh criterion indicates that accretion discs with strictly keplerian angular velocity profiles are hydrodynamically stable since

$$\frac{dj^2}{dr} > 0,$$

where $j = R^2\Omega$ and $\Omega = \sqrt{GM/R^3}$. More generally, a differentially rotating, compressible fluid with angular velocity varying with height and radius, $\Omega(R, Z)$, subject to axisymmetric isentropic perturbations (i.e. DS/Dt = 0, where D/Dt is the total time derivative for fluid elements) is stable if both of the Solberg-Høiland criteria are satisfied (e.g. Tassoul 1978):

$$\frac{1}{R^3} \frac{\partial j^2}{\partial R} + \frac{1}{\rho C_p} \left(-\nabla P \right) \cdot \nabla S > 0 \tag{20}$$

$$-\frac{\partial P}{\partial Z} \left(\frac{\partial j^2}{\partial R} \frac{\partial S}{\partial Z} - \frac{\partial j^2}{\partial Z} \frac{\partial S}{\partial R} \right) > 0. \tag{21}$$

Accretion disc models generally possess negative radial pressure gradients, and a negative vertical pressure gradient in the disc hemisphere above the midplane, leading to stability criteria (20) and (21) in the form:

$$\frac{1}{R^3} \frac{\partial j^2}{\partial R} + \frac{1}{\rho C_n} \left(\left| \frac{\partial P}{\partial R} \right| \frac{\partial S}{\partial R} + \left| \frac{\partial P}{\partial Z} \right| \frac{\partial S}{\partial Z} \right) > 0 \tag{22}$$

$$\frac{\partial j^2}{\partial R} \frac{\partial S}{\partial Z} - \frac{\partial j^2}{\partial Z} \frac{\partial S}{\partial R} > 0.$$
 (23)

Considering a disc with a strictly keplerian j profile we see that stability according to eqn. (23) requires $\partial S/\partial Z > 0$, in agreement

4 Nelson, Gressel & Umurhan

with the Schwarzschild condition for convective stability. Condition (22) shows that a large amplitude negative radial entropy gradient $\partial S/\partial R<0$ can also drive instability in principle, provided the gradient is strong enough to overcome the positive angular momentum gradient. This is distinct from the global baroclinic and/or subcritical baroclinic instability discussed in the introduction that does not require violation of the Solberg-Høiland criteria to operate, but does require thermal evolution of the fluid on time scales similar to the dynamical time to re-establish the initial radial entropy gradient, in addition to the presence of finite amplitude perturbations (Lesur & Papaloizou 2010).

Considering a quasi-keplerian disc whose angular velocity depends on height and radius, $\Omega(R, Z)$, eqn. (23) shows that such a disc with $\partial S/\partial Z > 0$ can be destabilised through the combination $(\partial j^2/\partial Z)(\partial S/\partial R) > 0$.

We consider two basic disc models in this paper that are the subject of nonlinear simulations in which the fluid evolution is isentropic and for which the Solberg-Høiland criteria determine hydrodynamic stability. One model assumes the temperature profile is a strict power law function of radius, R, such that the density and angular velocity are given by eqns. (12) and (13). With values p = -1.5 and q = -1, -0.5, -0.25 and 0 in eqns. (2) and (3), respectively, these discs are stable according to criterion (22). The term involving $\partial S/\partial R$ provides the only destabilising contribution (because $\partial S/\partial Z > 0$), but is always far too small to overcome the positive radial gradient in j^2 . This disc is also stable according to criterion (23) as $(\partial j^2/\partial R)(\partial S/\partial Z) > (\partial j^2/\partial Z < 0)(\partial S/\partial R)$.

The second set of disc models we consider assume that the entropy is a strict power law function of radius R. The density and angular velocity are given by the expressions (15) and (16), and the values (p=0, s=-1) and (p=-1.5, s=0) are adopted in eqns. (3) and (6). Both of these models are stable according to criterion (22) as the destabilising term proportional to $\partial S/\partial R$ is either zero or too small (note that $\partial S/\partial Z=0$ in these models). Criterion (23), however, predicts instability for the (p=0, s=-1) model because only the second term on the left-hand side is non zero, with $\partial j^2/\partial Z<0$ and $\partial S/\partial R<0$. The isentropic simulation that we present in the results section later in this paper will provide an example of nonlinear evolution of this model that is unstable according to one of the Solberg-Høiland criteria. The model with (p=-1.5, s=0) is stable according to criterion (23).

3.2 The Goldreich-Schubert-Fricke instability

When thermal and viscous diffusion play a role the stability of rotating flows are no longer controlled by the Solberg-Høiland criteria, but instead are determined by stability criteria obtained originally by Goldreich & Schubert (1967) and Fricke (1968) in application to the radiative zones of differentially rotating stars. Axisymmetric rotating flows are susceptible to the Goldreich-Schubert-Fricke (GSF) instability when viscous diffusion is much less efficient than thermal diffusion, such that a fluid element retains its initial angular momentum but quickly attains the entropy of the surrounding fluid when perturbed from its equilibrium location. Under these circumstances the stabilising influence of entropy gradients provided by the Solberg-Høiland criteria diminish and instability ensues for wave modes satisfying the instability criterion

$$\frac{\partial j^2}{\partial R} - \frac{k_R}{k_Z} \frac{\partial j^2}{\partial Z} < 0. \tag{24}$$

For a rotating flow where the angular momentum is a function of both *R* and *Z*, and the appropriate conditions on thermal and viscous

diffusion are satisfied, unstable modes are guaranteed to exist since wavevectors with ratios k_R/k_Z that satisfy eqn. (24) can always be found. In general, we expect $|\partial j/\partial R| \gg |\partial j/\partial Z|$ in a quasi-keplerian accretion disc, such that unstable modes will have $|k_R/k_Z| \gg 1$ (i.e. unstable modes will have radial wavelengths that are very much shorter than vertical ones).

Application of the GSF instability to accretion discs has not received a great deal of attention in the literature (but see the discussion below). Indeed, the study presented in this paper has arisen from unrelated attempts to generate 3D models of protoplanetary disc models within which turbulence is generated by the MRI in active layers near the disc surface, and in which extensive dead zones that are magnetically inactive (or at least stable against the MRI) exist near the midplane. The adoption of a locally isothermal equation of state in these models, combined with the absence of a physical viscosity, rendered them unstable to the growth of vertical corrugation oscillations that in the nonlinear regime became quite violent. This behaviour appears to be a nonlinear manifestation of the GSF instability, which we study here in more detail. The two classes of models we consider (temperature constant on cylinders and entropy constant on cylinders) both have angular velocity profiles that depend on both R and Z, and we expect that models in which perturbations evolve quasi-isothermally will display the GSF instability.

Previous analysis of the GSF instability in the context of accretion discs was initiated by Urpin & Brandenburg (1998) in which they presented a local linear analysis utilising the shortwavelength approximation. A more extensive analysis was presented in Urpin (2003) where it was suggested that the GSF may provide a source of hydrodynamic turbulence in accretion discs, and nonlinear simulations were presented by Arlt & Urpin (2004). These nonlinear simulations adopted a basic disc model with a strictly isothermal equation of state. As such, the underlying equilibrium disc model has an angular velocity profile that is independent of height, Z, (see eqn. 13) and should not be susceptible to the GSF instability. Arlt & Urpin (2004), however, adopted initial conditions that allowed relaxation around the equilibrium state leading to variations of Ω with height, and when initial perturbations with $|k_R/k_Z| \gg 1$ were applied growth of the GSF was observed. It is also worth noting the related linear and nonlinear study of isentropic accretion disc models presented by Rüdiger et al. (2002) at this point. This study examined the stability of discs whose angular momentum and entropy profiles rendered them stable according to the previously discussed Solberg-Høiland criteria. As expected, applied perturbations were found to always decay. We present a linear analysis of the instability we study in Sect. 6 for a fully compressible fluid under the assumption that the equation of state is locally isothermal, and in the appendix we present an analysis of the problem that closely follows the derivation of the GSF stability in Goldreich & Schubert (1967).

4 NUMERICAL METHODS

The simulations presented in this paper were performed using two different codes that utilise very different numerical schemes. We use an older version of NIRVANA, which uses an algorithm very similar to the ZEUS code to solve the equations of ideal MHD (Ziegler & Yorke 1997; Stone & Norman 1992). This scheme uses operator splitting, dividing the governing equations into source and transport terms. Advection is performed using the second-order monotonic transport scheme (van Leer 1977). We also use the more modern

Table 1. Simulation parameters and results. Labels beginning with a 'T' denote runs with T being a function of R. Those with a 'K' denotes runs where $K_s = K_s(R)$. The letter R denotes reflecting boundary conditions, and a letter O denotes outflow b.c's. Digits after the hyphens denote thermal relaxation times. Note that all runs have $H_0/R_0 = 0.05$.

Simulation	p	q or s	$ au_{ m Relax}$	$N_r \times N_\theta \times N_\phi$	Unstable ?
T1R/O-0	-1.5	-1	0.00	1328 × 1000 × 1	Y
T2R/O-0	-1.5	-0.5	0.00	$1328 \times 1000 \times 1$	Y
T3R/O-0	-1.5	-0.25	0.00	$1328 \times 1000 \times 1$	Y
T4R/O-0	-1.5	0	0.00	$1328 \times 1000 \times 1$	N
T5R-0.01	-1.5	-1	0.01	1328 × 1000 × 1	Y
T6R-0.1	-1.5	-1	0.10	$1328 \times 1000 \times 1$	N
T7R-1.0	-1.5	-1	1.00	$1328 \times 1000 \times 1$	N
T8R-10.0	-1.5	-1	10.0	$1328 \times 1000 \times 1$	N
T9R-∞	-1.5	-1	∞	$1328 \times 1000 \times 1$	N
K1R-0	0	-1	0.00	1328 × 1000 × 1	Y
K5R-0.01	0	-1	0.01	$1328 \times 1000 \times 1$	Y
K6R-0.1	0	-1	0.10	$1328 \times 1000 \times 1$	Y
K7R-1.0	0	-1	1.00	$1328 \times 1000 \times 1$	Y
K8R-10.0	0	-1	10.0	$1328 \times 1000 \times 1$	Y
K9R–∞	0	-1	∞	$1328 \times 1000 \times 1$	N
K10R-0.01	-1.5	0	0.01	$1328\times1000\times1$	N
T1R-0-3D	-1.5	-1	0.00	1328 × 1000 × 300	Y

NIRVANA-III code, which is a second order Godunov-type MHD code (Ziegler 2004), which has recently been extended to orthogonal-curvilinear coordinate systems (Ziegler 2011). All presented simulations were performed using a standard spherical coordinate system (r, θ, ϕ) .

4.1 Initial and boundary conditions

The numerical study presented here applies to the two general classes of disc model discussed in Sect. 2.1, and as such we adopt a numerical set up that is not specific to any particular physical system (although our motivation for undertaking this study arose from earlier attempts to establish stationary equilibrium solutions for protostellar disc models). Based on numerous test calculations performed with a wide range of resolutions during an early stage of this project, we know that the instability we study here is characterised by having a radial wavelength much shorter than the vertical wavelength (i.e. $k_R \gg k_Z$) during its early growth phase. Consequently we consider disc models with fairly narrow radial domains to facilitate high resolution simulations. The spherical polar grid we adopt has inner radius $r_{in} = R_0 = 1$ and outer radius $r_{out} = 2$, and most simulations we present are axisymmetric. The one nonaxisymmetric simulation we present covers a restricted azimuthal domain of $\pi/4$, again to facilitate a high resolution study.

Disc models in which the initial temperature is a strict function of cylindrical radius, R, have meridional domains $\pi/2 - 5H_0/R_0 \le \theta \le \pi/2 + 5H_0/R_0$. For a disc with radial temperature profile q = -1, corresponding to a disc with constant H/R, the meridional domain covers ± 5 scale heights above and below the midplane. For larger (less negative) values of q, the disc covers ± 5 scale heights at the inner radius, but a reduced number of scale heights as one moves out in radius. Prior to initiating these simulations, the disc models are specified using eqns. (3), (2), (12) and (13). In all models the initial velocity field was seeded with random noise distributed uni-

formly in each component with a peak amplitude equal to $1\,\%$ of the local sound speed.

Discs for which the initial entropy function, K_s , depends only on R have physical surfaces where the density goes to zero. In these models the meridional boundaries are placed at a location that is 5% smaller than the angular distance from the midplane where the density vanishes. The initial models are specified using eqns. (3), (6), (15) and (16). In order to determine the value of K_0 in eqn. (6), we specify the midplane Mach number, \mathcal{M}_{mid} , at radius R_0 . We adopt $\mathcal{M}_{\text{mid}} = 20$ to be consistent with the models for which H/R = 0.05. Seed noise with amplitude equal to 1% of the sound speed was again added to all velocity components.

For most simulations we adopt standard outflow or reflecting boundary conditions at the inner and outer radial boundaries. Periodic boundaries are applied in the azimuthal direction, and either standard outflow or reflecting conditions are applied at the meridional boundaries (all simulations performed using NIRVANA-III adopted outflow boundary conditions at the radial and merdional boundaries). The density is obtained in ghost zones by means of linear extrapolation. A variety of different boundary conditions were used in test simulations at an early stage of this project, and the results were found to be insensitive to the choice adopted. These tests included the adoption of damping boundary conditions that absorb incoming waves, indicating that reflecting boundaries are not required to drive the instability discussed in this paper.

Owing to the unsplit character of finite volume schemes, such as used in NIRVANA-III, it is difficult numerically to preserve static equilibria (Zingale et al. 2002). In particular, problems arise with the constant extrapolation of the density profile in the vertical direction. This is because the weight of the gas is not balanced by the now vanishing pressure gradient in the case of an isothermal equation of state, leading to a standing accretion shock in the first grid cell of the meridional domain. In the case of an adiabatic evolution equation, the same problem arises in the boundary condition for the thermal energy (which enters the boundary condition for the total energy). To alleviate this situation, we obtain the density (and in the case of solving an energy equation, the pressure) by integrating the hydrostatic equilibrium in each cell adjacent to the domain boundary. This is done with a second-order Runge-Kutta shooting method.

Unless indicated otherwise, we use a fixed resolution of $N_r \times N_\theta$ of 1328×1000 grid cells for our NIRVANA runs with $H_0/R_0 = 0.05$ or $\mathcal{M}_{\text{mid}} = 20$ at $r = R_0$. The NIRVANA-III runs used a resolution of 1344×1024

We adopt a system of units in which M = 1, G = 1 and $R_0 = 1$. When presenting our results, the unit of time is the orbital period at the disc inner edge, $P_{in} = 2\pi$.

5 RESULTS

The main aims of the following simulations are to delineate conditions under which the disc models outlined in Sect. 2.1 are unstable to the growth of the vertical shear instability, and to examine the effect that different physical and numerical set-ups have on the growth and evolution of this instability. We also aim to characterise the final saturated state of these unstable discs, although our adoption of mainly axisymmetric simulations provides some restriction in achieving this final aim.

We define the volume integrated meridional and radial kinetic

6 Nelson, Gressel & Umurhan

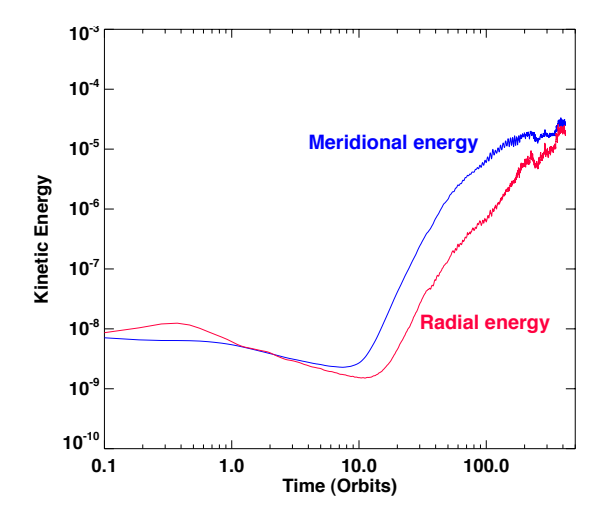


Figure 1. Time evolution of the normalised perturbed kinetic energy in the meridional and radial coordinate directions for model T1R-0 with p = -1.5, q = -1 and reflecting boundary conditions at the meridional boundaries.

energies through the expressions

$$e_{\theta} = \frac{1}{2} \int_{V} \rho v_{\theta}^2 dV, \quad e_r = \frac{1}{2} \int_{V} \rho v_r^2 dV. \tag{25}$$

When presenting our results we normalise these energies by the total kinetic energy contained in keplerian motion in the disc initially.

We begin discussion of our results below by describing simulations of locally isothermal discs for which $T(R) \sim R^{-q}$ and $\rho(R) \sim R^{-p}$. We describe one fiducial model in detail, before discussing briefly the influence of the temperature profile in controlling the instability. We present a comparision between results obtained using the two codes described in Sect. 4, and also demonstrate how the instability evolves as a function of disc viscosity.

The next set of results we present are for disc models in which the initial temperature is a strict function of R, but we set $\gamma=1.4$, solve the energy in eqn. (1), and allow the temperature to relax toward its initial value using eqn. (18). In this section, we examine how the thermal relaxation rate contols the instability, covering the full range of thermodynamic behaviour from locally isothermal through to isentropic.

In the penultimate part of our numerical study, we consider disc models for which the entropy function, K_s , is a strict function of R, and again employ thermal relaxation to examine the conditions under which accretion discs display the vertical shear instability. The final numerical experiment we present examines the instability in a full 3D model, and provides an estimate of the Reynolds stress induced by the instability.

We present an analytic model in the discussion section which illustrates the basic mechanism of the instability and delineates the conditions under which it operates.

5.1 A fiducial model

We begin presentation of the simulation results by discussing one particular model in detail to illustrate the nature of the instability that is the focus of this paper. The fiducial model is TR1–0 listed in Table 1, with temperature, T, defined as a function of R only, and p=-1.5 and q=-1 in eqns. (3) and (2). A locally isothermal equation of state is adopted. As such, this disc model has parameters very similar to those used in numerous previous studies of

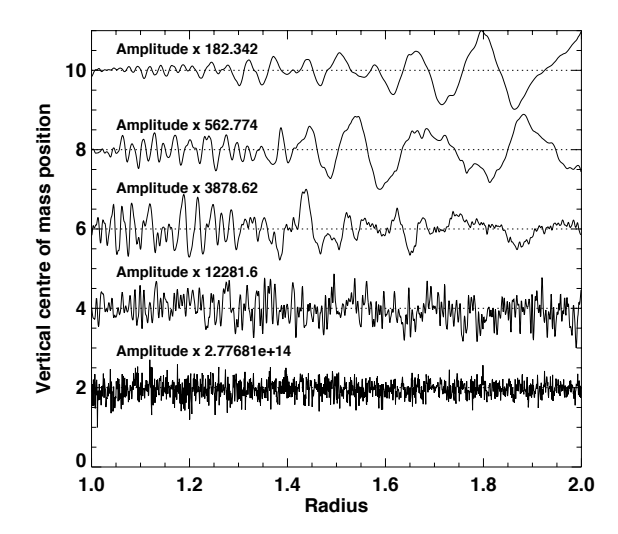


Figure 4. Time evolution of the vertical centre of mass position for each radial location in the disc for the fiducial model T1R–0 with H/R = 0.05. Note that the vertical centre of mass position has been normalised by the local scale height at each radius. Starting from bottom to top the plots correspond to times (in orbits): 9×10^{-4} , 9.18, 27.86, 65.00, 92.66. The multiplicative factor indicated in each legend causes the maximum amplitude of the normalised c.o.m. position in each graph to equal unity.

disc related phenomena (e.g. Kley et al. 2001; Cresswell & Nelson 2006; Fromang et al. 2011b; Pierens & Nelson 2010), although we focus primarily on the inviscid non-magnetised evolution here.

The time evolution of the normalised meridional and radial kinetic energies defined in eqn. (25) are shown in Fig. 1. The intial values at t=0 originate from the seed noise, and we observe that after ~ 10 orbits, during which the perturbed kinetic energies damp slightly, rapid growth of the perturbation energies arises. The normalised energies reach non linear saturation after ~ 400 orbits having reached values of a few $\times 10^{-5}$. Inspection of the evolution of the sum of the meridional plus radial kinetic on a log-linear plot indicates that the linear growth rate of the perturbed energy in Fig. 1 is $\simeq 0.24$ orbit⁻¹.

Contour plots of vertical velocity perturbations, v_Z , that arise at different stages of the disc evolution are shown in Figs. 2 and 3. These two figures show the perturbed velocity field at identical times, but whereas Fig. 2 maps linearly between the velocity values and the grey-scale, Fig. 3 plots the values $sign(v_z) \times |v_z|^{1/4}$ so that the grey-scale is stretched to enable the morphology of the perturbations to be more clearly discerned. Both figures demonstrate that perturbations start to grow near the upper and lower disc surfaces, where $|d\Omega/dZ|$ is largest, and toward the inner edge of the disc. The perturbations are characterised by having short radial and long vertical wavelengths, as expected for the vertical shear instability described in Sects. 3.2 and 6. The short radial wavelength gives rise to significant radial shear in the vertical velocity dv_Z/dR , and this apparently causes small scale eddies to form at the shearing interfaces. As time proceeds the instability extends toward the disc midplane and out to larger radii, until the entire disc participates in the instability (although it should be noted that the midplane where $d\Omega/dZ = 0$ is formally stable to local growth of the vertical shear

Close inspection of the lower panels in Fig. 3 show that the velocity perturbations have odd symmetry about the midplane initially (this is particularly apparent in the fourth panel between radii $1.1 \le r \le 1.4$). In other words the disc exhibits a breathing mo-

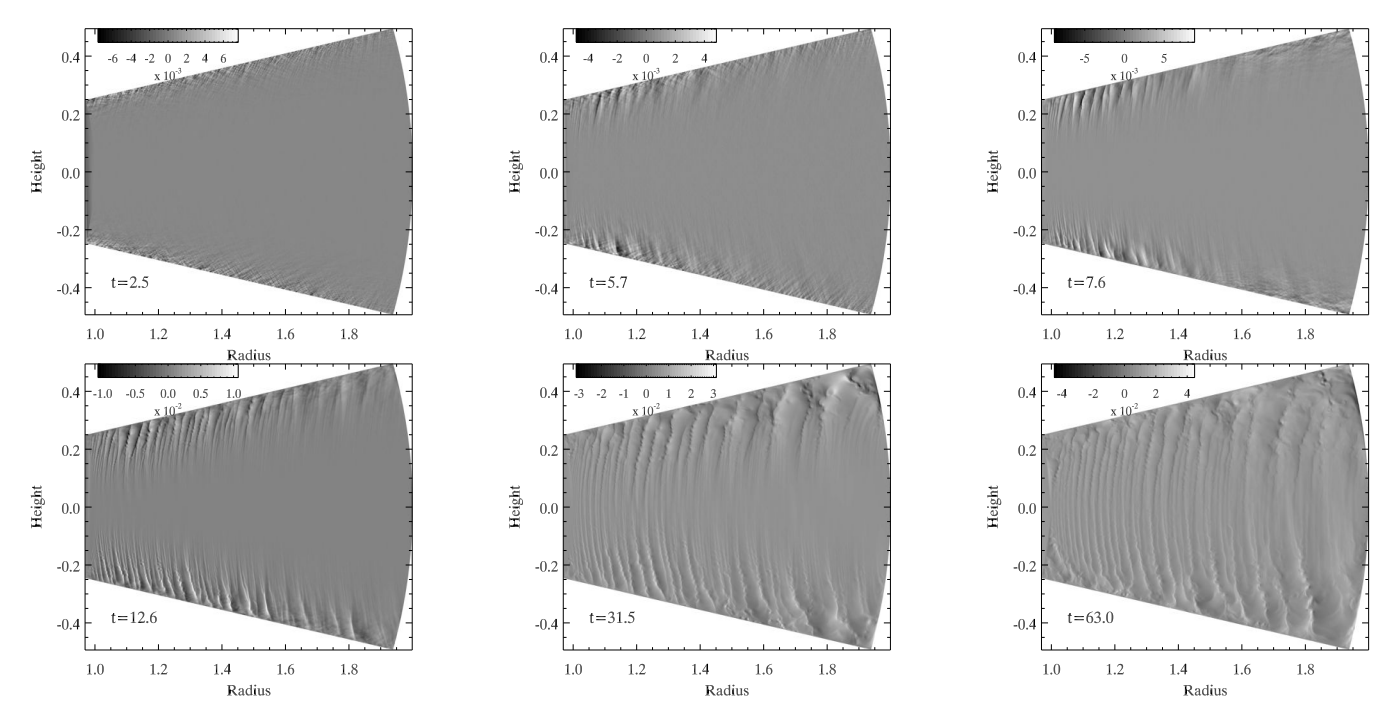


Figure 2. Edge-on contours of the perturbed vertical velocity as a function of R, Z and time for model T1R-0.

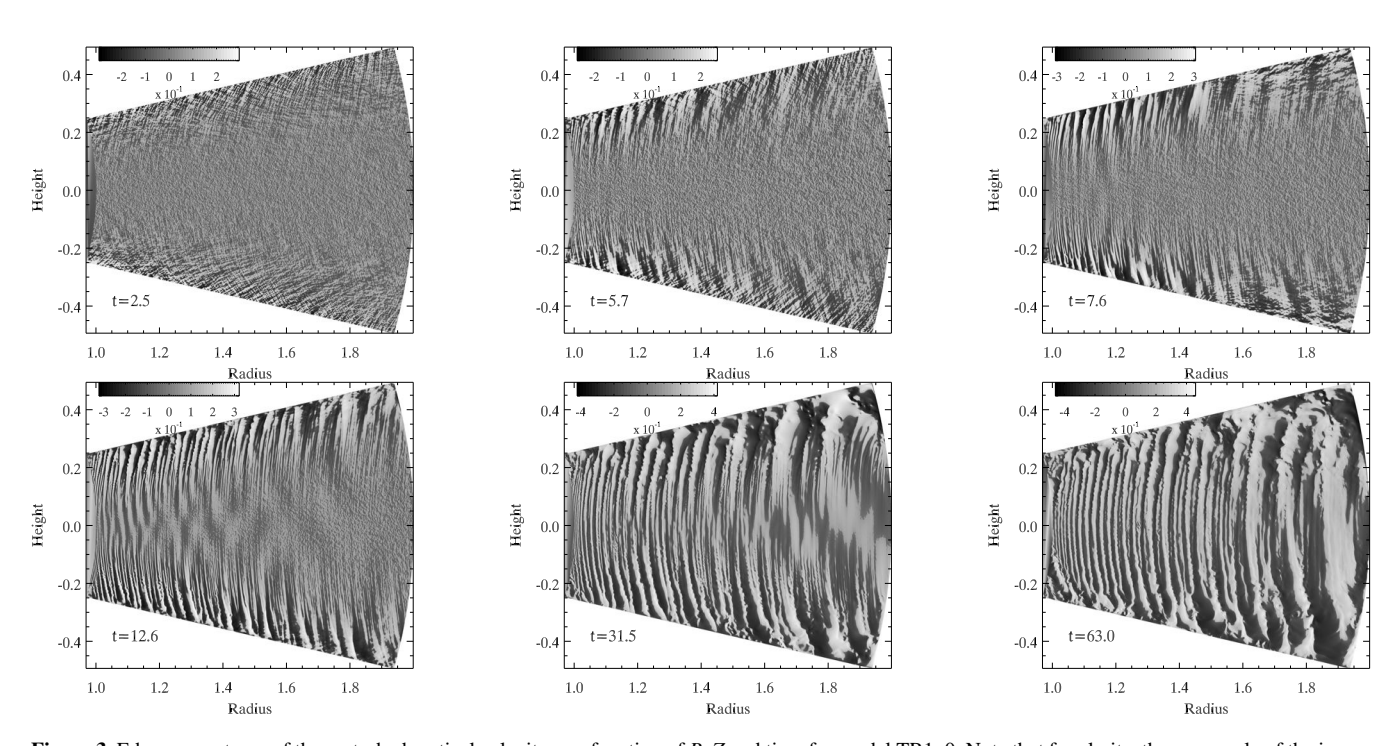


Figure 3. Edge-on contours of the perturbed vertical velocity as a function of R, Z and time for model TR1–0. Note that for clarity, the grey-scale of the image has been streteched by plotting the quantity $sign(v_Z) \times |v_Z|^{1/4}$. Note that the spectrum bar shows values of $v_Z^{1/4}$.

tion about the midplane as the instability first becomes apparent at lower disc latitudes. As time proceeds, however, the velocity perturbations become symmetric about the midplane as demonstrated by the fifth and sixth panels. These perturbations correspond to corrugation of the disc characterised by coherent oscillations of the vertical centre of mass position whose phase depends on radius in a time dependent manner. The development of this disc corrugation is illustrated by Fig. 4 which shows the vertical centre of mass po-

sition of the disc at each radius for five different times (note that each plot is off-set in the vertical direction to aid clarity, and each curve has been multiplied by a unique factor so that the corrugation may be observed). The vertical centre of mass has been normalised by the local disc scale height at each radius. Moving from the lower curve to the upper curve, we note that the vertical centre of mass position has a very small variation with radius after one time step, but this becomes progressively larger in amplitude and

8

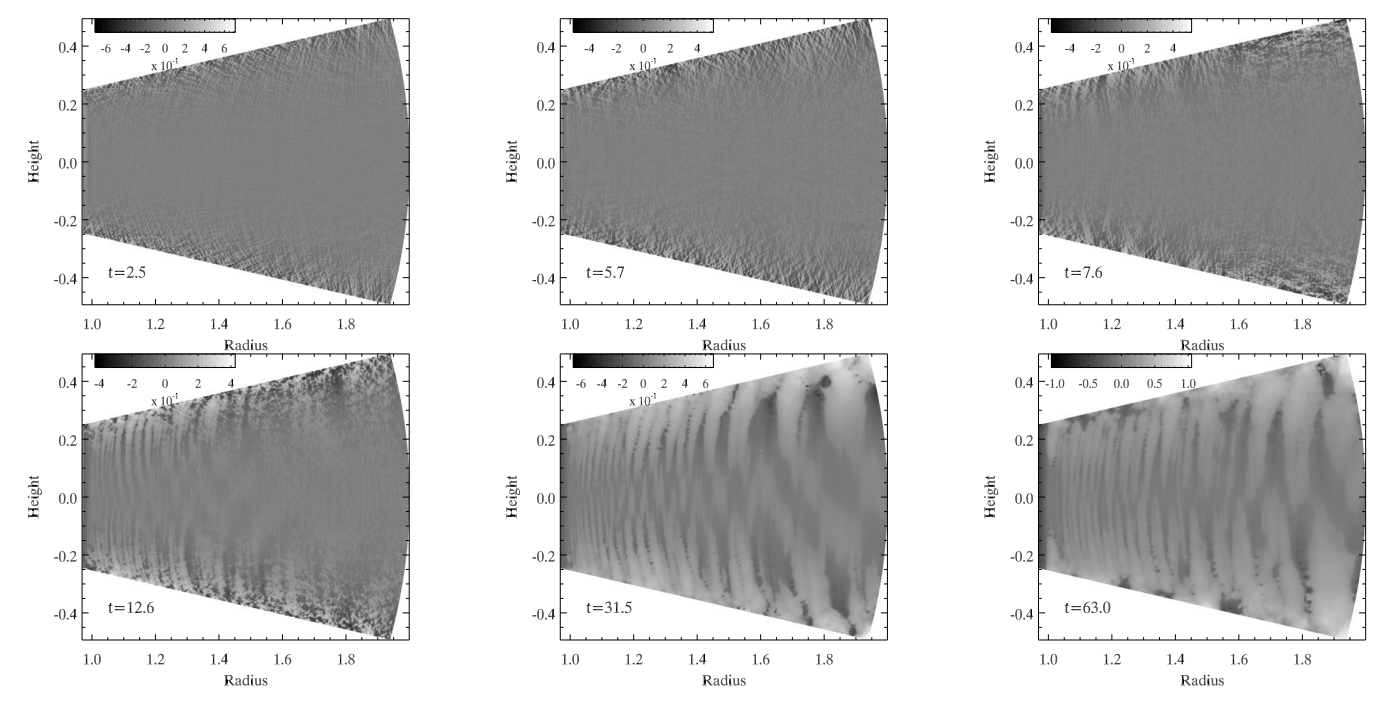


Figure 5. Edge-on contours of the disc relative density perturbations $\delta\rho/\rho_0$ as a function of R, Z and time. Note that we have effectively stretched the grey-scale by plotting the quantity $sign(\delta\rho) \times \sqrt{\delta\rho/\rho_0}$

more spatially coherent as time progresses (times corresponding to each curve are given in the figure caption). The final curve, corresponding to an evolution time of ~ 92 orbits, has a maximum vertical displacement approximately equal to 0.006H. It is interesting to note that the initial disc instability begins with $|k_R/k_Z|\gg 1$ due to the short radial wavelengths of the fastest growing modes of the vertical shear instability. As the disc approaches the nonlinear state, however, the development of coherent corrugation waves causes the radial wavelengths of the most apparent perturbations to approach or modestly exceed the local scale height. At the end of the simulation (~ 420 orbits) the maximum vertical displacement of the disc centre of mass reaches $\sim 0.01H$, but we are cautious about interpreting the results at this late stage of evolution as the reflecting boundary conditions may play a role.

Contour plots of the density perturbations $\delta\rho/\rho_0$ corresponding to the previously discussed velocity contours are displayed in Fig. 5. As with the velocity contours, we see perturbations first arise near the disc surface. Coherent density structures first become visible in the third panel, but are substantially more apparent in the lower panels.

The final saturated state consists of locally unstable disc annuli that oscillate vertically at close to the local frequency, $\Omega_k(R)$, superposed on which are a spectrum of oscillations with different frequencies caused by travelling waves excited by vertical oscillations at neighbouring disc radii. A region of the disc lying at intermediate radii will thus experience a locally generated corrugation, in addition to inward travelling corrugation waves that propagate as inertial modes (or r-modes) launched from exterior disc locations, and outward propagating corrugation waves propagating as acoustic or fundamental modes launched from interior disc locations (Lubow & Pringle 1993; Lubow & Ogilvie 1998).

Although we only present simulations with finite amplitude initial perturbations to the velocity fields in this paper, we have conducted numerous experiments in which the peak amplitude of the imposed perturbations varies, including cases where perturbations just grow from numerical round-off errors. Although this requires a larger time interval for the instability to become apparent, we nonetheless observe instability for all perturbation amplitudes, demonstrating that the instability is linear.

5.2 Evolution as a function of the radial temperature profile

In this section we discuss simulations T1R-0 to T4R-0 (which utilise reflecting boundary conditions in the meridional direction) and T1O-0 to T4O-0 (which use open boundary conditions). These simulations have p = -1.5 and a range of values for q running from q = -1 (a constant H/R disc) up to q = 0 (a purely isothermal disc in which $H/R \propto R^{1/2}$).

The left panel of Fig. 6 shows the time evolution of the normalised perturbed kinetic energy summed over the radial and merdional directions in the disc models T1R-0 to T4R-0. We see that as the value of q increases from q = -1 through to q = -0.25, the growth rate of the instability decreases, and for q = 0 it switches off altogether. Inspection of the evolution of the sum of the meridional and radial kinetic energies on a log-linear plot indicates that the linear growth rate for the q = -0.5 case is ≈ 0.12 orbit⁻¹, and for the q = -0.25 run is ≈ 0.052 orbit⁻¹ (to be contrasted with the growth rate $\simeq 0.24 \text{ orbit}^{-1}$ obtained for the q = -1 run). The azimuthal velocity in the q = 0 model is independent of Z, as indicated by eqn. (13), so the observed stability of this disc model is in agreement with the expectations discussed in Sect. 3. It is also noteworthy that the saturated values of the perturbation energies in each unstable disc, normalised to the total energy in keplerian motion, differ substantially from one another in accord with the trend in the growth rates.

The right panel of Fig. 6 shows the corrugation energies for runs T1O-0 to T4O-0, which are identical to runs T1R-0 to T4R-0 except that the boundary conditions applied at the meridional

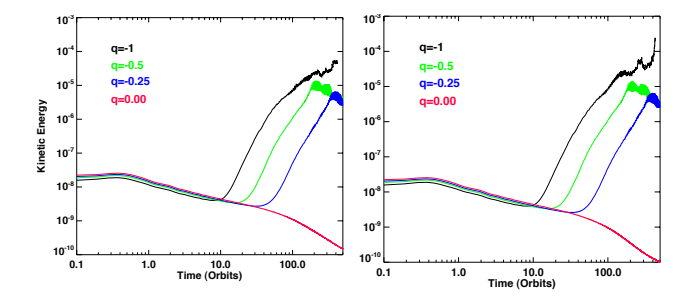


Figure 6. Time evolution of the perturbed meridional plus radial kinetic energies (normalised) as a function of the radial temperature profile. The left/right panel shows results for simulations which adopted reflecting/outflow boundary conditions at the upper and lower disc surfaces.

boundaries are outflow rather than reflecting. During the growth phase of the instability the results of the T10–0 – T40–0 runs are essentially identical to the corresponding T1R–0 – T4R–0 calculations, and the saturated energies are very similar. We also observe the important result that the transition between stable and unstable disc models is independent of the boundary conditions, with both q=0 models showing decay of the perturbed meridional and radial kinetic energies during the simulations. It is clear that the existence of a radial temperature profile plays a fundamental role in determining whether or not a disc becomes unstable.

5.3 Code comparison

Numerical modelling of the Navier-Stokes equations can pose arcane pitfalls, particularly if hydrodynamic instabilities are involved. In the absence of rigorous analytical reference solutions, it has become customary to substantiate the physical reliability of the solutions obtained by means of code comparisons. While we have already shown the generality of a GSF-like instability occurring under various physical settings, we demonstrate here its comparative development using two numerical schemes. Although very similar in their names, the two codes we used are fundamentally different in the numerical schemes they apply. NIRVANA utilises the same finite-difference scheme as the zeus code, whereas NIRVANA-III applies a finite-volume Godunov scheme very similar to the ones used in, e.g., RAMSES (Teyssier 2002) or ATHENA (Gardiner & Stone 2008).

We have run the simulations labelled as T1O-0 to T4O-0 in Table 1 using both codes. The codes generally agree well in the development of the instability and its saturation level as demonstrated by Fig. 7, although it should be noted that the realisation of the initial seed noise in the two runs is slightly different. The decay of these initial seed perturbations occurs slightly faster in the NIRVANA-III simulations, and the saturation amplitude is slightly smaller. A detailed look at the vertical velocity perturbations at time $t \simeq 12.8$ orbits is shown in Fig. 8, and both codes show the characteristic $|k_R/k_Z| \gg 1$ perturbations associated with the early development of the vertical shear instability. The codes are in decent agreement about the magnitude of the velocity perturbations and also in the dominant wavelength of instability. The codes, however, also show some differences in their solution at this time. The continued presence of the initial seed noise is more apparent in the NIRVANA run than in the NIRVANA-III run, in agreement with the evolution of the kinetic energies in Fig. 7, and the NIRVANA run shows a greater degree of structure in the velocity perturbations, perhaps indicative of higher-order modes being present at this time. Overall

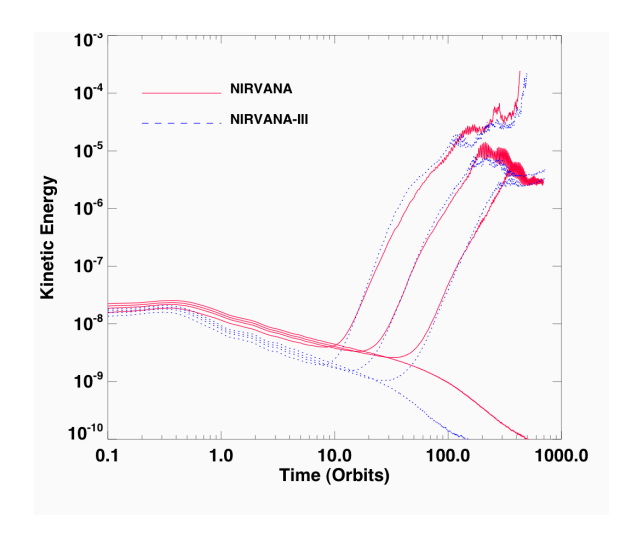


Figure 7. Comparison of the time evolution of the normalised (meridional + radial) kinetic energies for models T1O–0 to T4O–0 that were run with the two codes.

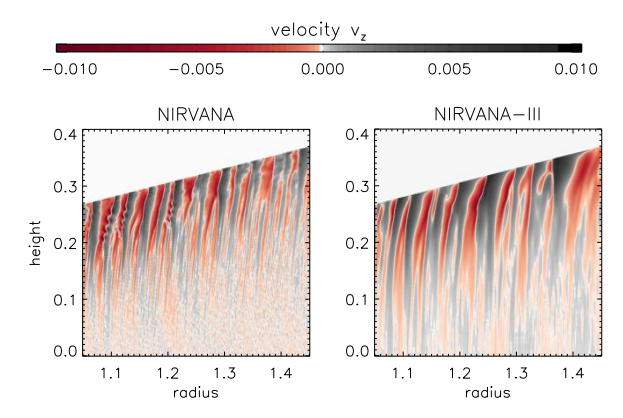


Figure 8. Comparison between the vertical velocity perturbations at time t = 12.8 orbits for the NIRVANA and NIRVANA-III runs. The results are for simulation T1O-0.

the comparision is very satisfactory and demonstrates that the conditions for the vertical shear instability to occur are predicted accurately by both numerical schemes, which also show reasonable agreement for the growth rates under different radial temperature profiles.

5.4 Evolution as a function of viscosity

In this section we present results from simulations that examine the amplitude of the saturated state as a function of imposed viscosity. We apply a constant kinematic viscosity, v, to the disc model T1R–0 and vary its value between $10^{-8} \le v \le 10^{-5}$ (a value of $v = 10^{-6}$ corresponds to the Shakura-Sunyaev viscous stress parameter $\alpha = 4 \times 10^{-4}$ at R = 1 (Shakura & Sunyaev 1973), and to a Reynolds number $Re = Hc_s/v = 2500$). The results are shown in Fig. 9, which shows the time evolution of the perturbed meridional plus radial kinetic energies. As expected, the results have a strong dependence on viscosity. For $v = 10^{-5}$ the instability is damped completely, which explains why previous 3D simulations of locally isothermal discs have not reported seeing the vertical shear instability (e.g. Kley et al. 2001; Cresswell & Nelson 2006; Fromang et al. 2011b; Pierens & Nelson 2010). For decreasing values of v

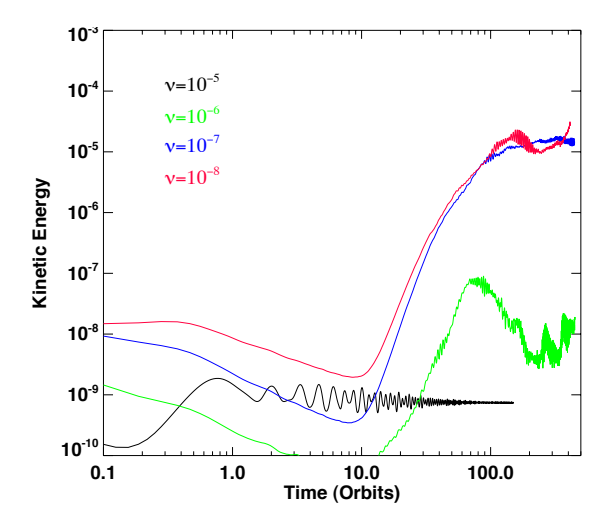


Figure 9. Time evolution of the normalised perturbed kinetic energy in the meridional and radial coordinate directions for model T1R–0 with p=-1.5, q=-1 and reflecting boundary conditions at the meridional boundaries. Each curve corresponds to a different value of the imposed kinematic viscosity, ν , as indicated.

the amplitude of instability increases, until at a value of $\nu = 10^{-8}$ there is little difference between the result in Fig. 9 and the inviscid result shown in the left panel of Fig.6.

Interestingly, it is found that in fully turbulent models where the MRI is active throughout the disc and $\alpha \simeq 0.01$, the corrugation instability is not observed (Fromang & Nelson 2006). We have computed models similar to those presented in Fromang & Nelson (2006) and find that corrugation of the disc does not develop. Although these MHD simulations adopt a significantly lower resolution than the pure hydrodynamic runs we have presented here, we note that hydrodynamic runs performed at low resolution still show the development of the instability even when the short radial wavelength perturbations of the initial growth phase are not resolved. Instead, we find that the disc displays longer wavelength breathing and corrugation modes that become unstable and cause the disc to oscillate vertically in quite a violent manner. In magnetised global disc models with dead zones whose vertical height covers $\simeq 2.5$ scale heights, which support Reynolds stresses in the dead zone with an effective value of $\alpha \simeq 10^{-4}$, the development of these corrugation oscillations is observed in models that adopt a locally isothermal equation of state with q = -1.

5.5 Thermal relaxation in models with T(R)

We now consider the evolution of models where we relax the locally isothermal assumption associated with the response of the fluid to perturbations. We evolve the energy equation in (1), and introduce thermal relaxation by integrating eqn. (18). We adopt the equation of state $P=(\gamma-1)e$, and set $\gamma=1.4$. The gas is assumed to be inviscid. Power-law profiles for the initial temperatures, T(R), and midplane density, $\rho_{\rm mid}(R)$, are adopted with q=-1 and p=-1.5 in eqns. (2) and (3). The aim of these models is to examine the robustness of the vertical shear instability as a function of the thermal relaxation time, $\tau_{\rm relax}$, defined in eqn. (18) and expressed as a fixed multiple or fraction of the local orbital period. These runs are labelled T5R-0.01 – T9R- ∞ in Table 1.

The evolution of the normalised perturbed kinetic energies for a number of models with relaxation times in the range $0 \leqslant \tau_{\rm relax} \leqslant$

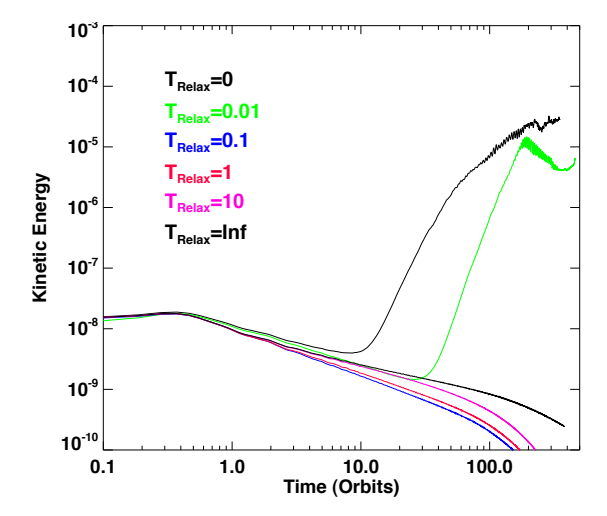


Figure 10. Time evolution of the sum of the (normalised) perturbed radial and meridional kinetic energy in discs where the temperature was initially constant on cylinders, as a function of the thermal relaxation time. Note that only the $\tau_{Relax}=0$ and 0.01 cases show growth.

 ∞ are plotted in Fig. 10. It is immediately obvious that instability only occurs in either the locally isothermal case ($\tau_{\rm relax}=0$) and when $\tau_{\rm relax}=0.01$ orbits. All other simulations result in the perturbed kinetic energy contained in the initial seed noise decaying with time. We note that the case of $\tau_{\rm relax}=\infty$ is directly comparable to a previous study on the adiabatic evolution of a stratified disc by Rüdiger et al. (2002). The authors considered the hydrodynamic stability under the Solberg-Høiland criterion and also find stability in this case.

Our results indicate that the vertical shear instability requires that the initial temperature profile of the fluid is re-established rather rapidly during dynamical evolution, at least for the equilibrium temperature and density profiles adopted in these particular models.

The requirement for near-isothermal evolution suggests that the vertical shear instability is most likely to operate in the optically thin regions of astrophysical discs whose global properties are similar to those considered here. For example, the outer regions of protoplanetary discs lying beyond ~ 50–100 AU may be prone to this instability, provided that MHD turbulence is present at low enough levels that the instability is not damped by the turbulent viscosity. This seems to be a likely prospect given that low density regions may be stabilised by ambipolar diffusion (Armitage 2011). It should also be noted, however, that the simple thermal relaxation model we employ does not capture the fact that the thermal evolution time of a mode with radial wavelength λ_R scales as $\sim \lambda_R^2/\mathcal{D}$ (where \mathcal{D} is the thermal diffusion coefficient), such that very short wavelength modes may remain unstable in optically thick discs. A reduction in spatial scales on which the instability operates, however, will presumably affect the resulting turbulent flow and reduce the associated Reynolds stress and transport coefficients in the nonlinear saturated state.

5.6 Thermal relaxation in models with $K_s(R)$

We now consider models in which the initial entropy function, $K_s(R)$, follows a strict power-law function of radius given by eqn. (6), and the midplane density, $\rho_{\text{mid}}(R)$, follows a radial power-law given by eqn. (3). For all models except one we adopt the val-

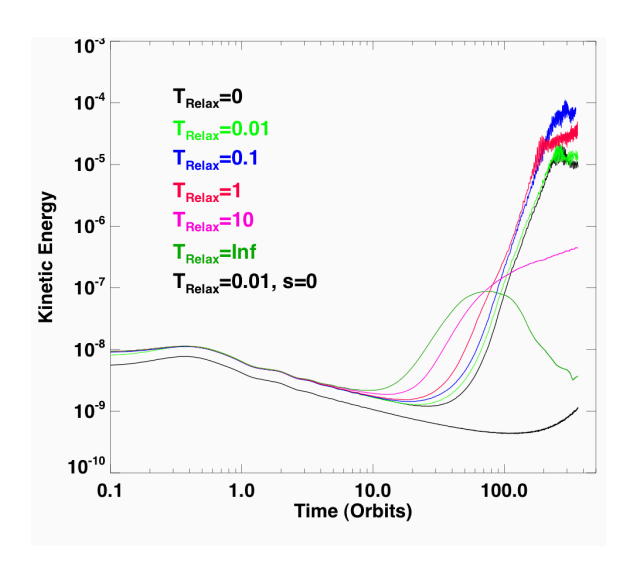


Figure 11. Time evolution of the sum of the normalised radial and meridional kinetic energies in discs where the entropy function, $K_s(R)$, was initially constant on cylinders.

ues s=-1 and p=0, leading to the midplane Mach number, \mathcal{M}_{mid} , being constant at all radii. Our normalisation of $K_s(R_0)$ sets $\mathcal{M}_{\text{mid}}=20$. We also consider a single model with p=-1.5 and s=0, so that there is no initial radial entropy gradient. The entropy in this case is normalised so that $\mathcal{M}_{\text{mid}}=20$ at $R=R_0=1$. These runs are listed in Table 1 as K1R-0 to K10R-0.01.

We impose reflecting conditions at the meridional boundaries, and consider inviscid evolution. As described in Sect. 2.1.1, these models are convenient to implement numerically because analytic solutions can be obtained for the equilibrium density and velocity field through eqns. (3) and (16). As such, these models allow us to explore the vertical shear instability as a function of the thermal relaxation time, $\tau_{\rm relax}$, in discs where the initial distribution of temperature no longer follows a power-law function of cylindrical radius, but instead varies with both R and R. We note that eqn. (16) also demonstrates that a radial power-law in $R_s(R)$ with $R_s(R)$ are an equilibrium $R_s(R)$ with $R_s(R)$ are an equilibrium $R_s(R)$ with $R_s(R)$ are an equilibrium $R_s(R)$ but adopting $R_s(R)$ implies that no vertical gradient in $R_s(R)$ exists.

The normalised sum of the radial and meridional kinetic energies is plotted in Fig. 11 for thermal relaxation times in the range $0 \le \tau_{\rm relax} \le \infty$ local orbits. The model with s=0 and p=-1.5 employed a relaxation time $\tau_{\rm relax}=0.01$ orbits, and is labelled as ' $T_{\rm relax}=0.01$, s=0'.

Interestingly, for the model with s=-1 and p=0, all values of $\tau_{\rm relax}$ result in growth of the perturbed meridional and radial energies, and only the strictly isentropic simulation with $\tau_{\rm relax}=\infty$ shows eventual decay over long time scales of ~ 100 orbits. It is noteworthy that this isentropic model is unstable according to one of the Solberg-Høiland criteria discussed in Sect. 3, and this is probably the cause of the initial growth in perturbed energy. The subsequent decay may arise because the instability causes the equilibrium disc to move to a stable state. Inspection of the perturbed velocity profiles in contour plots similar to Figs. 2 and 3 (not shown here) for all of the runs with p=0 and s=-1 shows that the previously discussed characteristic perturbations with $|k_R/k_Z|\gg 1$ grow initially, even for the isentropic disc model with no thermal relaxation. All models with finite thermal relaxation time show long term growth in perturbed energy, although in the case of $\tau_{\rm relax}=10$ or-

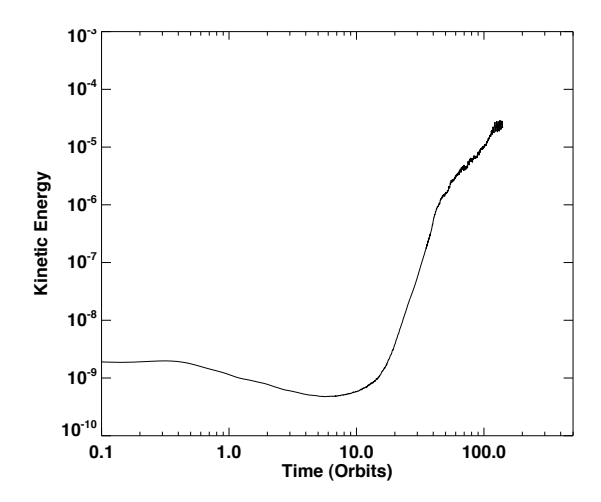


Figure 12. Time evolution of the perturbed meridional + radial kinetic energy (normalised by the total energy in keplerian motion) for the full 3D simulation T1R-0-3D.

bits the growth time is very long indeed. The instability displayed by the remaining models with $\tau_{\rm relax} \leqslant 10$ orbits shows that the requirement of very rapid thermal relaxation observed in the models presented in Sect. 5.5 actually depends on the detailed temperature and density structure of the disc. It is clear that disc models exist for which thermal relaxation times in the range $0 \leqslant \tau_{\rm relax} \leqslant 10$ orbits lead to the growth of the instability, and as such its range of applicability in the study of the dynamics of astrophysical discs is probably broader than suggested by the results presented in Sect. 5.5. A full exploration and understanding of the range of applicability, however, is beyond this paper, and will require a dedicated and detailed future study that accounts for the thermal evolution of the disc with greater realism.

Turning to the run with p=-1.5 and s=0, we see that the initial perturbation energy decreases for the first ~ 200 orbits before increasing again. The expectation is that this model will not display the vertical shear instability, and inspection of velocity contour plots (not shown here) confirms that the characteristic perturbations with $|k_R/k_Z| \gg 1$ do not appear in this case. These velocity plots, however, indicate that over secular time scales sound waves are generated close to the meridional boundaries, and this appears to be the reason for the up-turn in the perturbed kinetic energies seen in Fig. 11 after 200 orbits.

5.7 Non-axisymmetric model

We now consider briefly the evolution of a non-axisymmetric model T1R-0-3D, in which the azimuthal domain covered $\pi/4$ radians. This model is the 3D equivalent of model T1R-0. The simulation was performed using the NIRVANA code, and the model was set up using equations (3), (2) and (13), with values p = -1.5 and q = -1. The velocity field was seeded with noise (amplitude $0.01c_s$). Details of the model are given in Table 1.

The total normalised kinetic energy (meridional + radial) versus time is displayed in Fig. 12. Comparing with the equivalent axisymmetric plot (Fig.6) we see that the evolution is similar, with growth in the perturbed energy occurring after ~ 10 orbits, and saturation at a value of a few $\times 10^{-5}$ beginning to occur after ~ 100 orbits.

In Fig. 13 we plot the time evolution of the volume averaged Reynolds stress normalised by the mean pressure in the disc. This

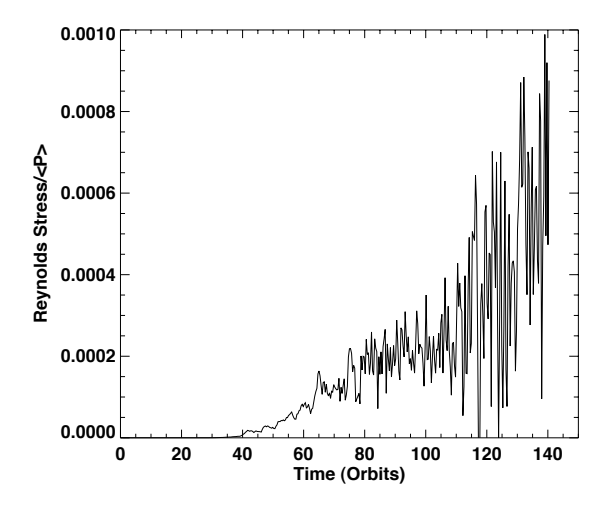


Figure 13. Time evolution of the volume averaged Reynolds stress (normalised by the mean pressure) for the full 3D simulations T1R-0-3D

quantity is computed as follows. We define an azimuthally averaged Reynolds stress $T_{\rm R}(r,\theta)$ obtained by averaging the quantity $\rho\delta\nu_{\rm R}\delta\nu_{\phi}$ over azimuth. Here $\delta\nu_{\rm R}$ and $\delta\nu_{\phi}$ are the local radial and azimuthal velocity fluctuations. We also define a density-weighted mean pressure as a function of $r, \overline{P}(r)$, obtained by averging over θ and ϕ . We define a local value of the Shakura-Sunyaev stress parameter $\alpha(r,\theta) = T_{\rm R}(r,\theta)/\overline{P}(r)$. The simple average of $\alpha(r,\theta)$ over r and θ is the quantity plotted in Fig. 13.

Although rather noisy, we see that the normalised stress approaches average values $\sim 6 \times 10^{-4}$ by the end of the simulation (and appears to be still growing at this point). The spatial distribution of $\alpha(r,\theta)$, time averaged during the last 10 orbits of the run, is shown in Fig. 14. Here we see that local values of the stress reach $\sim 2 \times 10^{-3}$, indicating that the vertical shear instability generates a quasi-turbulent flow capable of supporting significant outward angular momentum transport in astrophysical discs, given favourable conditions for its development.

The upper panels of Fig. 15 show contours of the perturbed density, $\delta\rho/\rho_0$ in a slice parallel the meridional plane at three different times during the simulation, showing similar features to those presented for the 2D-axisymmetric simulation in Fig. 5. Perhaps more interesting are the lower panels of Fig. 15 which show the actual density ρ in the (R,ϕ) plane located at the disc midplane. Here the development of spiral density waves may be observed, similar in morphology to those that arise in discs where turbulence is driven by the MRI (e.g. Papaloizou & Nelson 2003). The 3D simulation presented here suggests that if the appropriate conditions prevail in astrophysical discs, the vertical shear instability may lead to a turbulent flow capable of supporting significant angular momentum transport.

6 THEORETICAL CONSIDERATIONS

The GSF instability appears by rendering the inertial modes of a rotating atmosphere unstable. The original analysis in Goldreich & Schubert (1967, GS67 hereafter) demonstrated the possibility of this instability by performing a point analysis at a given location in a stellar radiative zone away from the equator, equivalent to considering a location away from the midplane in a disc. In this section we examine the mathematical structure of the instability by further

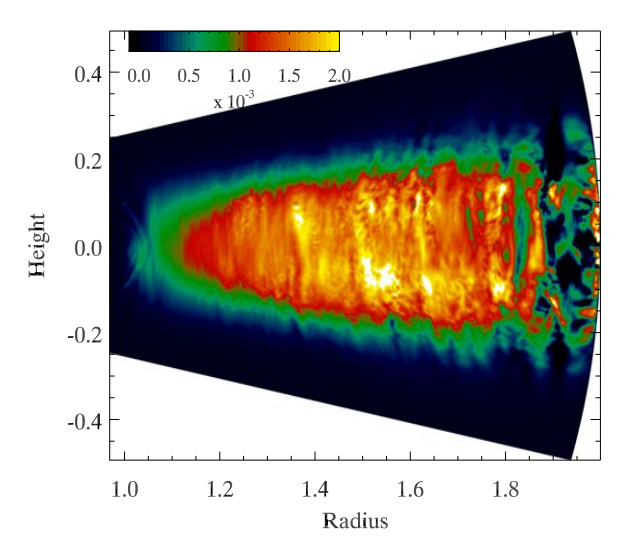


Figure 14. Spatial distribution of the time and horizontally averaged Reynolds stress (normalised by the mean pressure at each radius) for the model T1R-0-3D.

extending previous analyses, including those of Urpin (2003) and Arlt & Urpin (2004), by relaxing the point assumption.

We shall focus on disturbances which are locally isothermal. For the sake of completion of this important discussion we redo the original point analysis of GS67 in Appendix A, but without introducing the Boussineq approximation. Denoting σ as the growth rate we find that the inertial mode response is roughly given by

$$\sigma^2 = \frac{-\kappa_0^2 (c_0^2 k_z^2 + N_0^2) + 2\Omega_0 c_0^2 k_r k_z \frac{\partial \bar{V}}{\partial z}}{c_0^2 (k_z^2 + k_r^2) + \kappa_0^2 + N_0^2},\tag{26}$$

in which c_0 is the reference sound speed, κ_0 is the epicyclic frequency which, for a keplerian disc, is given by Ω_0 , the local keplerian rotation rate at the point in question. k_z and k_r are the corresponding vertical and radial disturbance wavenumbers respectively. The local Brunt-Vaisaila frequency is N_0 and $\partial \bar{V}/\partial z$ is the vertical gradient of the mean keplerian flow. This quantity typically scales on the order of magnitude of $(q/2)\Omega_0(H_0/R_0)$ where q is the same exponent of the radially varying isothermal sound speed discussed in Section 2. Supposing for this discussion that N_0 is negligible it follows from this expression that if H_0/R_0 is small then instability can only happen if the radial wavenumber conspires to be correspondingly large. In that limit the above expression implies

$$\sigma^2 \sim 2\Omega_0 \frac{k_z}{k_r} \frac{\partial \bar{V}}{\partial z} - \kappa_0^2 \frac{k_z^2}{k_r^2},\tag{27}$$

indicating that instability is possible if $k_z/k_r \sim O(qH_0/R_0)$. The analysis of Arlt & Urpin (2004), for example, also similarly indicates that for the same rough conditions the growth rate ought to scale as $O(q\Omega_0H_0/R_0)$. The simulations we have performed are consistent with this tendency where the radial length scales of the emerging structures are significantly shorter than the vertical ones with growth rates of the instability on the order of 4 orbit times for $H_0/R_0 \sim 1/20$ and q = -1.

Our goal is to develop a better physical understanding of the processes responsible for this instability beyond invoking Solberg-Høiland criteria. In this respect we notice from Figure 1 that radial velocity fluctuations are considerably smaller in magnitude than the corresponding meridional velocities.

With these clues in mind, we show in the following how the processes involved in bringing about the instability is largely

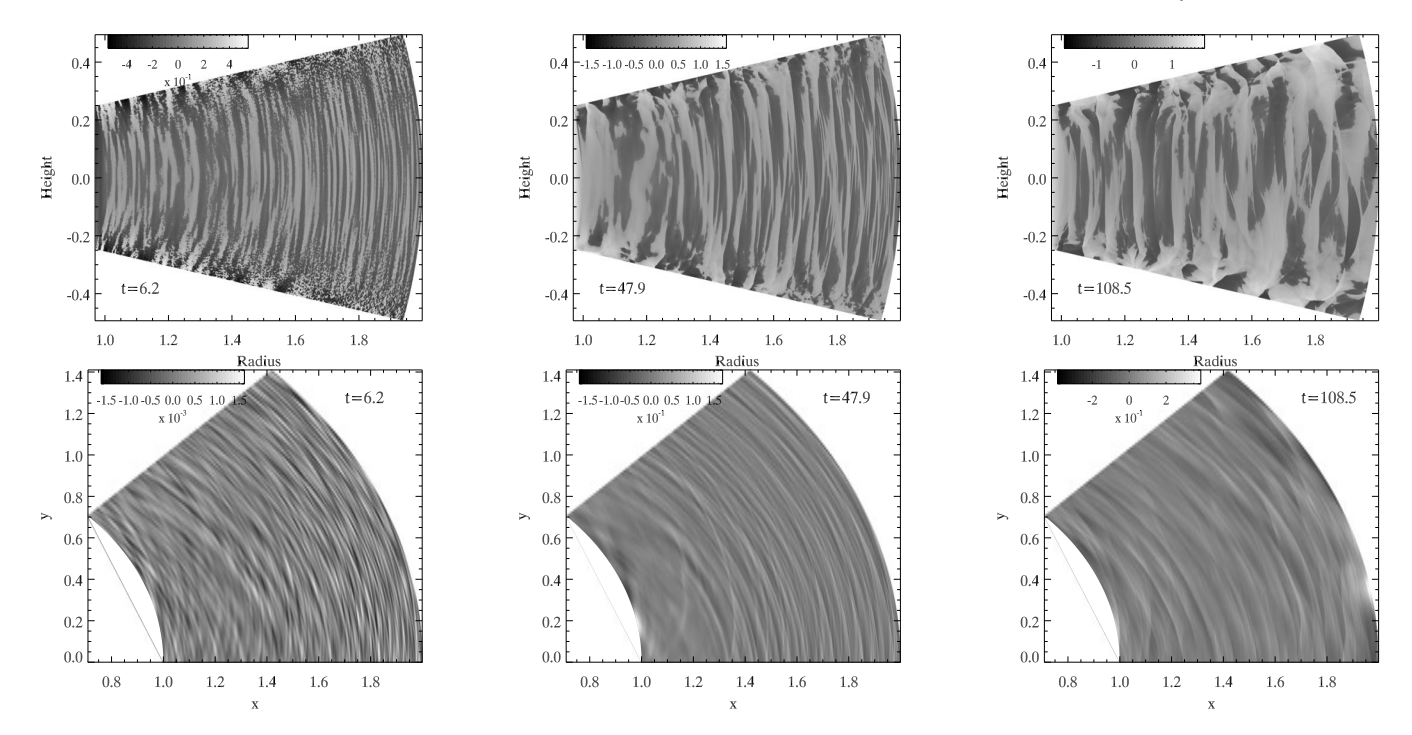


Figure 15. Perturbed density, $\delta\rho/\bar{\rho}$ in the merdional plane at $\phi = \pi/8$ (upper three panels) for the 3D simulation T1R-0-3D. Note that we have effectively stretched the grey-scale by plotting the quantity $sign(\delta\rho) \times |\delta\rho/\bar{\rho}|^{1/4}$ in the upper panels. The lower panels show the relative density perturbations $\delta\rho/\bar{\rho}$ at the disc midplane. No grey-scale stretching has been applied to these lower panels.

anelastic and radially geostrophic - by the latter expression we mean to indicate dynamics which are in constant radial force balance between Coriolis effects and pressure gradients. Furthermore, despite the varied simplifications we make to expose the essence of the physical process, the fundamental equations describing the resulting linearised response remain inseparable in the radial and vertical coordinates. This means that the only recourse in establishing any insight is through a further approximate solution of the resulting reduced equations. We find that the solution indicates that for given parameters describing disturbances the instability appears in pairs, as opposed to appearing individually as indicated by (27). Although we have not proved it in this study, we conjecture the powerful driving of the instability in the simulations may be, in part, caused by this feature.

6.1 Equations of motion revisited and steady states rederived

The equations of motion for axisymmetric inviscid dynamics in a cylindrical geometry are given by

$$\left(\frac{\partial}{\partial t} + U \frac{\partial}{\partial R} + W \frac{\partial}{\partial Z}\right) U - \frac{V^2}{R} = -\frac{1}{\rho} \frac{\partial c_s^2 \rho}{\partial R} - \frac{\partial \Phi}{\partial R},\tag{28}$$

$$\left(\frac{\partial}{\partial t} + U \frac{\partial}{\partial R} + W \frac{\partial}{\partial Z}\right) V + \frac{UV}{R} = 0, \tag{29}$$

$$\left(\frac{\partial}{\partial t} + U \frac{\partial}{\partial R} + W \frac{\partial}{\partial Z}\right) W = -\frac{1}{\rho} \frac{\partial c_s^2 \rho}{\partial Z} - \frac{\partial \Phi}{\partial Z}.$$
 (30)

Note that the (R, ϕ, Z) velocity components are given here by (U, V, W). We dispense with the subscripted scheme (v_r, v_ϕ, v_Z) used in previous sections in order to simplify the notation. The corresponding equation of mass continuity is

$$\frac{\partial \rho}{\partial t} + \frac{1}{R} \frac{\partial R \rho U}{\partial r} + \frac{\partial \rho W}{\partial Z} = 0. \tag{31}$$

As mentioned above, we focus here on dynamics that are locally isothermal with an infinitely short cooling time $(\tau_{\rm relax} \to 0)$. This then is to be considered in the context of simulations T1R-0 to T4R-0 summarized in Table 1. Reciting therefore from Section 2: it means that the square of the sound speed is given by $c_s^2 = c_0^2 (R/R_0)^q$ where R_0 is the fiducial reference disc position and c_0 is the scaled sound speed at that point. The gravitational potential emanating from the central object is $\Phi = -GM/(R^2 + Z^2)^{1/2}$.

The general equilibrium state solutions are found in eqns. (12)-(13) but, as we mentioned earlier, perturbations superposed on this base state are difficult to analyse because the resulting equations are fundamentally inseparable so that a typical normal-mode analysis is out of the question. In order to facilitate some kind of tractable analysis we make the one and only approximation here: the radial and vertical gradients of the potential Φ are expressed in terms of their corresponding first order Taylor Series expansions, i.e.

$$\begin{split} \frac{\partial \Phi}{\partial R} &\approx -\frac{GM}{R_0^2} \left(\frac{R_0}{R}\right)^2 = -\Omega_0^2 R_0 \left(\frac{R_0}{R}\right)^2, \\ \frac{\partial \Phi}{\partial Z} &\approx -\frac{GM}{R_0^3} \left(\frac{R_0}{R}\right)^3 Z = -\Omega_0^2 \left(\frac{R_0}{R}\right)^3 Z, \end{split}$$

in which $\Omega_0 = (GM/R_0^3)^{1/2}$ is the reference keplerian rotation rate at radius R_0 . The midplane density is chosen to be of the form $\rho_{mid} = \rho_0 (R/R_0)^p$ where ρ_0 is the reference density and where p is an arbitrary index (as referenced earlier). In the following analysis it will be convenient for our discussion to refer to the natural logarithm of the density instead of directly to the density itself, thus, we define $\Pi \equiv \ln \rho$. Because we shall be concerned with perturbations around the steady states implied by the above equations we shall

represent these states by overbars. As such, we have that

$$\overline{\Pi} = \ln \rho_{mid} - \frac{1}{2} \frac{Z^2}{H_0^2} \left(\frac{1}{\mathcal{H}^2} \right), \tag{32}$$

$$\overline{V} = \Omega_0 R_0 \left(\frac{R}{R_0}\right)^{-3/2} \left[1 + \varepsilon(R) + \frac{q}{4} \left(\frac{H_0}{R_0}\right)^2 \left(\frac{Z}{H_0}\right)^2 \left(\frac{R}{R_0}\right)^{-2}\right], (33)$$

where $H_0 \equiv c_0/\Omega_0$ is the local vertical scale height as referenced near the end of Section 2. The non-dimensionalised scale height \mathcal{H} is accordingly given via the relationship $\mathcal{H}^2 \equiv (R/R_0)^{3+q}$ also as found in Sect. 2. The nondimensional quantity ε is given by

$$\varepsilon \equiv \left(\frac{H_0}{R_0}\right)^2 C^2 \left(\frac{R}{R_0}\right) \left[R_0 \frac{\partial \ln \rho_{mid}}{\partial R} + R_0 \frac{\partial \ln C^2}{\partial R}\right]$$
$$= (p+q) \left(\frac{H_0}{R_0}\right)^2 \left(\frac{R}{R_0}\right)^{1+q}.$$

where $C^2 \equiv (R/R_0)^q$.

6.2 Linearised perturbations and non-dimensionalisation

We introduce perturbations by writing for each dependent quantity

$$U \to u', \qquad V \to \overline{V} + v', \qquad W \to w', \qquad \Pi \to \overline{\Pi} + \Pi',$$

and inserting these into the governing equations (28)-(31). Linearising results in the expressions

$$\frac{\partial u'}{\partial t} - 2\frac{\overline{V}}{R}v' = -c_s^2 \frac{\partial \Pi'}{\partial R},$$

$$\frac{\partial v'}{\partial t} + u'\frac{1}{R}\frac{\partial R\overline{V}}{\partial R} + w'\frac{\partial \overline{V}}{\partial Z} = 0,$$

$$\frac{\partial w'}{\partial t} = -c_s^2 \frac{\partial \Pi'}{\partial Z},$$
(34)

and

$$\frac{\partial \Pi'}{\partial t} = -\frac{1}{R} \frac{\partial Ru'}{\partial R} + \frac{\partial w'}{\partial Z} - u' \frac{\partial \overline{\Pi}}{\partial R} - w' \frac{\partial \overline{\Pi}}{\partial Z}.$$
 (35)

It will now be made more transparent if we non-dimensionalise the above equations according to the quantities appearing. We see that a natural time unit is given by the keplerian rotation time Ω_0^{-1} . The radial and vertical length scales are naturally scaled by R_0 and H_0 respectively. Thus we write for the these quantities

$$t \to \Omega_0^{-1} t, \qquad Z \to H_0 z, \qquad R \to R_0 r,$$
 (36)

where t, r, z are the corresponding non-dimensionalisations of the independent variables representing respectively time, radius and height. It is very important to note that the radial and vertical length scales are disparate with respect to each other by a factor of H_0/R_0 . Because in all of our simulations this ratio is quite small (~ 0.05) we shall treat this ratio as one of our "small parameters" and formally represent it by $\epsilon \equiv H_0/R_0$ (not to be confused with $\epsilon(R)$ defined earlier). This disparity must be kept in mind when the scalings invoked to recover the GSF instaiblity are formally made in the next section.

Judging from the dynamics observed in the simulations the structures appearing tend to be radially and vertically constrained. These spatial constraints (especially the radial confinement) indicate that perturbation velocities ought not to exceed the sound speed (at least initially). This is typical of the scalings frequently used to derive equations appropriate to the dynamics in a small box of a disk (Goldreich & Lynden-Bell 1965; Umurhan & Regev 2004) although we are not, technically, considering the dynamics

on such small scales yet. In sum, therefore, we scale the dependent perturbation velocities by

$$u' \to c_0 u, \qquad v' \to c_0 v, \qquad w' \to c_0 w,$$

where, as before, u, v, w represent the corresponding nondimensionalised component velocities in the radial, azimuthal and vertical directions. Therefore, the perturbation equations now take on the following more transparent appearance

$$\frac{\partial u}{\partial t} = 2\frac{\bar{v}}{r}v - \epsilon r^q \frac{\partial \Pi'}{\partial r},\tag{37}$$

$$\frac{\partial v}{\partial t} = -u \frac{1}{r} \frac{\partial r \overline{v}}{\partial r} - \epsilon w \left(\frac{1}{2} q z r^{-7/2} \right)$$
 (38)

$$\frac{\partial w}{\partial t} = -r^q \frac{\partial \Pi'}{\partial z},\tag{39}$$

and

$$\frac{\partial \Pi'}{\partial t} = -\epsilon \left(\frac{u}{r} + \frac{\partial u}{\partial r} \right) - \epsilon \frac{\partial \overline{\Pi}}{\partial r} u - \frac{\partial w}{\partial z} - w \frac{\partial \overline{\Pi}}{\partial z}, \tag{40}$$

where the non-dimensionalisation of the mean azimuthal flow \overline{V} is given in terms of the other redefined variables

$$\overline{\Pi} = \frac{p}{r} - z^2 \frac{1}{2\mathcal{H}^2},$$

$$\overline{v} = \frac{\overline{V}}{\Omega_0 R_0} = r^{-3/2} \left(1 + \varepsilon(r) + \frac{q}{4} \epsilon^2 z^2 r^{-2} \right),$$
(41)

with $\varepsilon(r) = \epsilon^2(p+q)r^{1+q}$ and $\mathcal{H}^2(r) = r^{3+q}$. We have written (38) in a seemingly curious way: the last term on the RHS of that equation is the product of the vertical gradient of the mean azimuthal flow term, i.e. $-w\partial \overline{v}/\partial z$. We have chosen to write it out explicitly in order to bring to the fore the leading order scaling that sits in front of it as it will effect how we proceed toward the reduced model (see the next section).

6.3 Asymptotic scalings and resulting reduced equations

The linearised equations of motion (37)-(40) are, despite our efforts to simplify, still inseparable between the r and z variables. In order to proceed asymptotically we must make further scaling choices. These are guided by both the results of the numerical solutions as well as by the discussion at the beginning of Section 6. At this stage we shall list them once again:

- (i) As estabilished by GS67, Urpin (2003) and Arlt & Urpin (2004), growth rates scale as $\sim q\Omega_0H_0/R_0$ which is, in our non-dimensionalised time units, $\sim \epsilon q$,
- (ii) For growth rates slow on the timescale of the local disc rotation, the emerging structures have radial dimensions (ℓ_r) considerably smaller than the corresponding vertical dimensions (ℓ_z). That is to say, for $\epsilon q \ll 1$ the scaling analysis of both GSF67 and Urpin (2003) indicate that $\ell_r/\ell_z \ll 1$
- (iii) The numerical solutions also clearly indicate that during the growth of the instability the radial velocity fluctuations are significantly smaller than the corresponding meridional velocity fluctuations (see Figure 1).

In the following we describe scalings of (37)-(40) that simplify them into a set which is both more transparent and more amenable to further analysis while retaining the essential physical processes involved in the instability. We assume that $\epsilon \ll 1$ and treat q as an order 1 quantity (although a more general analysis can be done without this a priori assumption achieving, in the

end, much of the same results discussed hereafter). Furthermore we consider the analysis around the fiducial radius r = 1. Since interest is in radial scales that are much smaller than the vertical scales and recalling that the r scales dimensionally represent physical length scales that are *longer* than the dimensional vertical scales z by a factor of ϵ^{-1} (= $R_0/H_0 \sim 20$) we consider radial disturbances

$$r-1=\epsilon^2 x$$

where x is order 1. We leave the z scales untouched as these are the de-facto reference scales of the analysis. Because the growth rates are long by a factor of ϵ^{-1} we introduce a new long-time variable τ given by

$$t = \tau \epsilon^{-1}$$
.

With this long-time scale assumed we find that in order to bring about non-trivial pressure balancing with the inertial term in the vertical momentum equation it must follow that the pressure fluctuations must relatively scale by ϵ as well. This can be easily surmised by examining (39) and noticing that for w order 1 and the time derivative scaling as order ϵ , that the only way balance occurs is if the pressure is correspondingly small by a factor of ϵ . This means introducing a new pressure fluctuation reflecting this scaling through

$$\Pi' = \epsilon \tilde{\Pi}$$
.

where $\tilde{\Pi}$ is the scaled pressure.

Finally as we have just intimated, in addition to the vertical velocity being order 1 we assume that the azimuthal velocity fluctuations are also unscaled (i.e. remaining order 1) in accordance with our numerical observations. We note here that scaling v to be order 1 is also consistent with the pressure scalings assumed because it leads to a balance between the radial pressure gradient and the Coriolis term in (37).

However, we suppose that the radial velocities are small in comparison to the other velocity components and we propose that its relative smallness is similar to the pressure field's scaling, i.e.

$$u = \epsilon \tilde{u}$$
.

where \tilde{u} is the correspondingly scaled radial velocity. Applying these scalings assumptions to eqns. (37)-(40) results in the following equations at lowest order,

$$0 = 2\nu - \frac{\partial \tilde{\Pi}}{\partial x},\tag{42}$$

$$\frac{\partial v}{\partial \tau} = -\frac{1}{2}\tilde{u} - \frac{1}{2}qzw, \tag{43}$$

$$\frac{\partial w}{\partial \tau} = -\frac{\partial \tilde{\Pi}}{\partial z}, \qquad (44)$$

$$0 = \frac{\partial \tilde{u}}{\partial x} + \frac{\partial w}{\partial z} - zw, \qquad (45)$$

$$0 = \frac{\partial \tilde{u}}{\partial x} + \frac{\partial w}{\partial z} - zw, \tag{45}$$

with corrections to the above equations appearing at order ϵ^2 . In this form these reduced equations contain insight with regards to two very important physical implications. The first of these follows from the interpretation of eqn. (42) which says that the dynamics of the instability occur under radially geostrophic conditions, that is to say, that the processes develop under conditions in which radial Coriolis effects balance radial pressure gradients. The second observation is that the linear dynamics are anelastic rather than incompressible in character. By this we mean to say the following: since on these radial/vertical length scales the mean (scaled) density profile has the form $\bar{\rho} = e^{-z^2/2}$, eqn. (45) may be equivalently

written as

$$\frac{\partial \bar{\rho}\tilde{u}}{\partial x} + \frac{\partial \bar{\rho}w}{\partial z} = 0. \tag{46}$$

The fact that the dynamics here are not incompressible in the usual sense is perhaps less surprising given that vertical stratification is non-negligible under these spatial constraints - had we been interested in vertical scales that were equally as short as the radial scales then stratification would not figure prominently.

The other two equations describing the vertical and azimuthal momentum balances retain their inertial terms and are largely unaffected (directly) by these scalings.

Before analyzing the solutions to these equations it is important to keep in mind that the essential effect giving rise to the instability is present in the guise of the final term on the RHS of eqn. (43). Additionally, in reflecting upon these equations, it should be kept in mind that \tilde{u} and $\tilde{\Pi}$ indicate real quantities that are intrinsically smaller (but not zero) compared to the other terms.

Approximate solutions and double instability

The reduced system (42-45) may be combined into a single equation for the pressure perturbation $\tilde{\Pi}$:

$$\frac{\partial^2}{\partial \tau^2} \frac{\partial^2 \tilde{\Pi}}{\partial x^2} = -\frac{\partial^2 \tilde{\Pi}}{\partial z^2} + \left(1 + q \frac{\partial}{\partial x}\right) z \frac{\partial \tilde{\Pi}}{\partial z}.$$
 (47)

We note here that a point analysis of (47), i.e., assuming $z = z_0$ is fixed and making a wave ansatz and proceeding similarly to Appendix A recovers the content of the asymptotic growth rates contained in eqn. (27), indicating the consistency of the scaling arguments we have exploited to get to this point.

Nonetheless, examination of this equation, although appearing quite simple in many respects, shows that it is also fundamentally inseparable owing to the $q\partial/\partial x$ term on the RHS of the expression. A more concerted future analysis is necessary to develop proper solutions of these equations subject to proper boundary conditions on both the vertical and radial boundaries of the system. However, we may proceed analytically by the following rationale.

Keeping in mind that that equation (32) says that the basic state density profile $\bar{\rho}$ has the form $\sim e^{-z^2/2}$ we can develop solutions of these equations in which we require that

- (i) The pressure fluctuations $\tilde{\Pi}$ are zero on the radial boundaries located at $x = \pm \Delta$ and,
- (ii) The kinetic energy in the fluctuations decay as $z \to \pm \infty$. Since the kinetic energy involves terms that are appear as $\bar{\rho}\tilde{u}^2, \bar{\rho}v^2$ and $\overline{\rho}w^2$ then this boundary condition is satisfied even if the velocity fields show *algebraic growth* as $z \to \pm \infty$.

The first boundary condition is not the same as the no-normal flow boundary conditions of the simulations but we have checked and found that the resulting growth rates and qualitative results are unchanged when implementing those conditions instead (see footnote later). This second condition is not outright unphysical but it, nevertheless, does not mirror the conditions present in the simulations and we must keep this in mind when we analyse the results later on. We assume all fields have normal-mode form in time

$$\tilde{\Pi}(x,z,t) = \hat{\Pi}(x,z)e^{s\tau} + c.c.$$

where s is the growth rate. This form is also assumed for the other variables \tilde{u}, v, w . As a side note we point out that with this solution ansatz inserted into eqn. (44) it follows that $s\hat{w} = -\partial_z \hat{\Pi}$. The equation for $\hat{\Pi}$ becomes

$$s^2 \frac{\partial^2 \hat{\Pi}}{\partial x^2} = -\frac{\partial^2 \hat{\Pi}}{\partial z^2} + \left(1 + q \frac{\partial}{\partial x}\right) z \frac{\partial \hat{\Pi}}{\partial z}.$$
 (48)

We proceed to develop solutions of (48) guided by the methods used to develop solutions to Hermite and Gegenbauer differential equations (Morse & Feshbach 1953; Lin 2012). With *m* a positive integer we assume a tractable non-separable solution of the following form

$$\hat{\Pi}(x,z) = \sum_{i=0}^{m} \hat{\Pi}_{jm}(x)z^{m},$$
(49)

where the radial functions $\hat{\Pi}_{jm}(x)$ are yet to be determined. ¹ Inserting this solution ansatz into (48) reveals that for a given m and for each index $j = \cdots, m-4, m-2$ the following equations must be satisfied

$$s^2 \frac{\partial^2 \hat{\Pi}_{jm}}{\partial x^2} = -(j+2)(j+1)\hat{\Pi}_{j+2,m} + j\hat{\Pi}_{jm} + qj\frac{\partial \hat{\Pi}_{jm}}{\partial x}.$$
 (50)

together with the corresponding "top" equation, i.e. the ordinary differential equation for j = m,

$$s^2 \frac{\partial^2 \hat{\Pi}_{mm}}{\partial x^2} = m \hat{\Pi}_{mm} + qm \frac{\partial \hat{\Pi}_{mm}}{\partial x}.$$
 (51)

The index j starts from 0 (1) depending if m is even (odd). In relation to the modes observed in our numerical solutions: breathing modes correspond to even values of m while corrugation modes correspond to odd values of m. We also note that each function $\hat{\Pi}_{jm}(x)$ must individually satisfy the boundary condition $\hat{\Pi}_{jm}(\pm \Delta) = 0$ for each j. This is a rather cumbersome task and it is not our intention here to fully develop detailed solutions. Rather, we seek to determine the value of the growth rate s which may be calculated by solving the top equation (51) subject to the boundary condition $\hat{\Pi}_{mm}(\pm \Delta) = 0$. Elementary analysis of this equation indicates solutions are of the form

$$\hat{\Pi}_{mm} = A_m e^{mx/s^2} \cos kx, \qquad k = n\frac{\pi}{2}, \text{ where } n = 1, 2, \cdots$$
 (52)

where A_m is an arbitrary constant. The requirement for the consistency of this solution follows from inserting (52) directly into (51) which, after factoring out $\hat{\Pi}_{mm}$ reveals the growth-rate relationship for s

$$s^4 + \frac{m}{k^2}s^2 + \frac{q^2m^2}{4k^4} = 0, (53)$$

which has solution

$$s^{2} = \frac{m}{k^{2}} \left(-1 \pm \sqrt{1 - q^{2}k^{2}} \right). \tag{54}$$

It follows from an examination of the above equation that for 0 < qk < 1 the two roots possible for s^2 are both negative which implies that the four modes are all oscillatory. However, instability is possible once qk > 1 since it implies that s^2 is now a complex number with a non-zero real part. Moreover, because of the sign convention, for qk > 1 there are always a pair of unstable modes and a pair of stable modes. In other words we always have in that case the four possible combinations: $s = \pm (|s_r| \pm i|s_i|)$ for some real

values of s_r , $s_i > 0$. This quality holds also for no-normal boundary conditions at $x = \pm \Delta$. For unstable values (|kq| > 1) the expressions $|s_r|$ and $|s_i|$ are given by

$$|s_r| = \frac{\sqrt{m/2}}{|k|} \sqrt{|kq| - 1}, \qquad |s_i| = \frac{\sqrt{m/2}}{|k|} \sqrt{|kq| + 1}.$$
 (55)

An elementary examination of the growth rate s_r shows that the wavenumber corresponding to maximal growth occurs for |kq| = 2. If we let λ_{max} denote the corresponding wavelength in *dimensional units* then this wavelength of maximal growth is

$$\lambda_{\max} = \pi R_0 \left(\frac{H_0}{R_0} \right)^2,$$

where, for our expreriments corresponding to $q=-1, H_0/R_0=0.05$, implies radial scales on the order of $\lambda_{\rm max}\sim 0.008R_0$. These scales are approximately the length scales observed at the early stages of growth in both Figures 2 and 3, especially near the $R_0=1$ boundary. Similarly, the growth rate of the fastest growing mode denoted by $\Re e(s_{\rm max})=|q|\sqrt{m/2}/2$ and, in dimensional units, this implies a maximum growth rate $\sigma_{\rm max}$

$$\sigma_{\max} = \frac{|q|\sqrt{m}}{2\sqrt{2}} \left(\frac{H_0}{R_0}\right) \Omega_0 = \sqrt{m}|q| \frac{\pi}{\sqrt{2}} \left(\frac{H_0}{R_0}\right) \text{orbit}^{-1}.$$

For the simulations T1R–0 to T4R–0 (Table 1) this means a maximum growth rate given by $\sigma_{\rm max} \sim 0.11 |q| \sqrt{m}$ orbit⁻¹. It should be kept in mind that these growth rates are for the individual velocity fields. However, the growth rates reported in Sect. 5 are for the perturbation kinetic energies which depend upon the square of the velocity fields. As such, the linear theory therefore predicts the maximum growth rates for the kinetic energy perturbations to $\sim 2\sigma_{\rm max}$ which, if applied to our numerical experiments, would be

$$\sim 0.22|q|\sqrt{m} \text{ orbit}^{-1}$$
.

This is significant since we reported there that the growth times were measured to be ~ 0.24 orbit⁻¹. The theory predicts: for the fundamental corrugation mode m=1 a growth rate of ~ 0.22 orbit⁻¹, while for the first breathing mode m=2 a growth rate of ~ 0.31 orbit⁻¹. This suggests that the growth rates observed in the early stages of growth of simulations T1R–0 to T4R–0 is a convolution of these two fundamental modes of the system.

The theory, as it stands, does not select for a preferred value of m as the growth rates all scale as \sqrt{m} suggesting curiously that for larger values of m one should expect faster growth rates. This appears to be in conflict with the original point analysis of GS67 and others. In particular, since m roughly indicates the number of nodes in the vertical direction one can treat m as a proxy for the vertical wavenumber k_z . But according to the criterion obtained via the point analysis (27), increasing the vertical wavenumber ought to promote stability. This conflict of interpretation needs to be resolved in follow up work, however, we do offer two hypotheses regarding this matter:

(i) Since the instability appears to be global in character (as evinced by the numerical solutions) that the classical point analyses serve only as a useful guide toward indicating the possibility of

¹ For example, when developing solutions to the Hermite differential equation of some integer order, the constant coefficients in front of each power of z are are determined through a standard recursive procedure in descending powers of z. The same is done here except that the recursive procedure generates coupled ordinary differential equations in x.

² In this case, after inserting the solution ansatz into the top equation (43) indicates that the no-normal boundary condition is enforced by requiring $s^2 \partial_x \hat{\Pi}_{nm} - qm \hat{\Pi}_{mm} = 0$ at $x = \pm \Delta$. What emerges is a more complicated relationship between s and k, m but resulting in the *same* qualitative features discussed for fixed pressure conditions. A more thorough exposition awaits a subsequent study.

instability only. Additionally, since the reduced equations derived here are more global in reach, it would be logically more appropriate to be guided by their content in better describing the emergence of the instability and/or,

(ii) The implementation of the decaying kinetic energy boundary condition for $z \to \pm \infty$ may be somehow responsible for the feature regarding m and the mode's stability character. It could be that high m modes may become stable if one, instead, imposes no normal flow conditions at some finite height away from the disc midplane. Of course, to do this requires non-trivial solution forms that are far more complicated than the solution ansatz assumed in (49).

7 DISCUSSION AND CONCLUSION

We have presented the results from a large suite of 2Daxisymmetric and 3D simulations, using two independent hydrodynamic codes, that examine the stability and dynamics of accretion disc models in which the temperature or entropy are strict functions of cylindrical radius. Such thermal profiles lead to equilibrium angular velocity profiles that depend on radius and height. We find that these disc models are unstable to the growth of modes with $|k_R/k_Z| \gg 1$ when the thermal evolution time is comparable to or shorter than the dynamical time. This mode pattern is expected for systems undergoing the Goldreich-Schubert-Fricke instability. The potential for this vertical shear instability to apply to accretion discs has been investigated previously by Urpin & Brandenburg (1998), Urpin (2003) and Arlt & Urpin (2004) using the Boussinesq approximation, and we have confirmed this with our own analysis that applies to fully compressible flows. The nonlinear simulations indicate that evolution of the instability leads to the dominant radial wavelength increasing from a fraction of the scale height during early times to being comparable to the scale height at later times. Instability also appears to generate disc vertical motions that correspond to vertical breathing modes at early times, but at later times the dominant motion corresponds to corrugation of the disc causing the disc midplane to oscillate around its initial location at all radii (at least in axisymmetric flows). A full 3D simulation computed using a locally isothermal equation of state indicates that the instability generates a turbulent flow in its nonlinear saturated state, leading to non-negligible transport of angular momentum through a Reynolds stress with corresponding viscous alpha value $\alpha \sim 10^{-3}$.

The requirement for quite rapid thermal evolution of the disc for strong instability to ensue suggests that the outer regions of protoplanetary discs may be places where this instability operates because of the low density and optical depth there. We caution that the thermal evolution time required for instability may depend on thermal gradients, such that instability can operate for longer cooling times in discs with steeper temperature/entropy profiles, but it seems unlikely that instability can be sustained if the local thermal time scale greatly exceeds a few orbital periods. We have shown that the instability is damped in viscous flows with dimensionless kinematic viscosity $v \ge 10^{-6}$, so these outer disc regions would need to be stable against the MRI for the instability to operate (the instability is not observed in global simulations of discs supporting fully developed MHD turbulence). It is likely that the MRI is quenched by ambipolar diffusion in the outermost regions of protostellar discs (Armitage 2011), so these may provide low density, magnetically inactive regions where the vertical shear instability can operate efficiently.

The vertical shear instability is an example of a baroclinic in-

stability because the required vertical shear in a disc only occurs if the pressure is a function of both density and pressure, $P(\rho, T)$. An important question that we have not addressed in this work is how a disc would evolve that is subject to both the vertical shear instability and the subcritical baroclinic instability (SBI) studied by Petersen et al. (2007) and Lesur & Papaloizou (2010). The conditions required for the SBI to operate and be sustained strongly are a radial entropy gradient and a fairly rapid thermal relaxation time, and we have shown that the vertical shear instability operates under these conditions also. Both Petersen et al. (2007) and Lesur & Papaloizou (2010) report that a strongly sustained instability is obtained for thermal time scales close to the local orbital period, leading to a highly complex flow in which long-lived vortices are formed, and an effective viscous stress of $\alpha \sim \text{few} \times 10^{-3}$ is maintained by the Reynolds stress in compressible flows. The 3D simulation we presented in Sect. 5.7 used a locally isothermal equation of state, and so is not subject to the SBI, but it seems likely that the combined action of the two instabilities in a disc with longer thermal evolution time and appropriate entropy gradient will generate a complex flow containing long-lived vortices and vertical motions that correspond to corrugation of the disc, accompanied by a Reynolds stress that leads to efficient outward angular momentum transfer. It is worth noting that the vertical shear instability is linear, whereas the SBI is a finite-amplitude instability, so it is possible that the SBI may be stimulated by perturbations generted during the development of the vertical shear instability. We will present a study of these two instabilities operating in tandem in a future publication to explore these hypotheses. Given the role that vortices may play in the trapping of solids during planet formation (e.g. Barge & Sommeria 1995; Klahr & Bodenheimer 2003), this is clearly an important issue for further investigation.

ACKNOWLEDGEMENTS

Part of this work used the NIRVANA-III code developed by Udo Ziegler at the Leibniz Institute for Astrophysics (AIP). All computations were performed on the QMUL HPC facility, purchased under the SRIF and CIF initiatives. We acknowledge the hospitality of the Isaac Newton Institute for Mathematical Sciences, where much of the work presented in this paper was completed during the 'Dynamics of Discs and Planets' research programme. RPN acknowledges useful and informative discussions with Steve Lubow on the subject of corrugation modes in discs during an early phase of this project. We acknowledge comments provided by the referee of an earlier version of this work that have led to substantial improvements in this paper.

REFERENCES

Arlt R., Urpin V., 2004, A&A, 426, 755 Armitage P. J., 2011, ARA&A, 49, 195 Balbus S. A., Hawley J. F., 1991, ApJ, 376, 214 Barge P., Sommeria J., 1995, A&A, 295, L1 Beckwith K., Armitage P. J., Simon J. B., 2011, MNRAS, 416, 361 Cameron A. G. W., Pine M. R., 1973, Icarus, 18, 377 Cresswell P., Dirksen G., Kley W., Nelson R. P., 2007, A&A, 473,

Cresswell P., Nelson R. P., 2006, A&A, 450, 833 D'Angelo G., Lubow S. H., 2010, ApJ, 724, 730 Fragner M. M., Nelson R. P., 2010, A&A, 511, A77+ Fricke K., 1968, ZAp, 68, 317

Fromang S., Lyra W., Masset F., 2011a, A&A, 534, A107

Fromang S., Lyra W., Masset F., 2011b, ArXiv e-prints

Fromang S., Nelson R. P., 2006, A&A, 457, 343

Gardiner T. A., Stone J. M., 2008, JCoPh, 227, 4123

Goldreich P., Lynden-Bell D., 1965, MNRAS, 130, 125

Goldreich P., Schubert G., 1967, ApJ, 150, 571

Hawley J. F., Balbus S. A., 1991, ApJ, 376, 223

Johnson B. M., Gammie C. F., 2006, ApJ, 636, 63

Klahr H. H., Bodenheimer P., 2003, ApJ, 582, 869

Kley W., D'Angelo G., Henning T., 2001, ApJ, 547, 457

Lesur G., Papaloizou J. C. B., 2010, A&A, 513, A60+

Lin D. N. C., Papaloizou J., 1980, MNRAS, 191, 37

Lin D. N. C., Pringle J. E., 1987, MNRAS, 225, 607

Lin M.-K., 2012, ApJ, 754, 21

Lubow S. H., Ogilvie G. I., 1998, ApJ, 504, 983

Lubow S. H., Pringle J. E., 1993, ApJ, 409, 360

Lynden-Bell D., Pringle J. E., 1974, MNRAS, 168, 603

Morse P., Feshbach H., 1953, Methods of Theoretical Physics Bind 1. McGraw-Hill

Papaloizou J. C., Savonije G. J., 1991, MNRAS, 248, 353

Papaloizou J. C. B., Nelson R. P., 2003, MNRAS, 339, 983

Papaloizou J. C. B., Pringle J. E., 1984, MNRAS, 208, 721

Petersen M. R., Stewart G. R., Julien K., 2007, ApJ, 658, 1252

Pierens A., Nelson R. P., 2010, A&A, 520, A14+

Ruden S. P., Papaloizou J. C. B., Lin D. N. C., 1988, ApJ, 329, 739

Rüdiger G., Arlt R., Shalybkov D., 2002, A&A, 391, 781

Ryu D., Goodman J., 1992, ApJ, 388, 438

Shakura N. I., Sunyaev R. A., 1973, A&A, 24, 337

Stone J. M., Norman M. L., 1992, ApJS, 80, 753

Takeuchi T., Lin D. N. C., 2002, ApJ, 581, 1344

Tassoul J.-L., 1978, Theory of rotating stars

Teyssier R., 2002, A&A, 385, 337

Toomre A., 1964, ApJ, 139, 1217

Umurhan O. M., Regev O., 2004, A&A, 427, 855

Urpin V., 2003, A&A, 404, 397

Urpin V., Brandenburg A., 1998, MNRAS, 294, 399

van Leer B., 1977, Journal of Computational Physics, 23, 276

Ziegler U., 2004, JCoPh, 196, 393

Ziegler U., 2011, Journal of Computational Physics, 230, 1035

Ziegler U., Yorke H. W., 1997, Computer Physics Communications, 101, 54

Zingale M., Dursi L. J., ZuHone J., Calder A. C., Fryxell B., Plewa T., Truran J. W., Caceres A., Olson K., Ricker P. M., Riley K., Rosner R., Siegel A., Timmes F. X., Vladimirova N., 2002, ApJS, 143, 539

APPENDIX A: RECITAL OF GS67 WITH LOCAL ISOTHERMAL ASSUMPTION

Owing to the importance of the original study presented by GS67, we repeat here the calculation contained in that work wherein we assume the equation of state of the gas is locally isothermal with a temperature profile varying in the nominal radial direction. We also extend that analysis to include the effects of compressibility and we do *not* assume outright that the hydrodynamic flow is incompressible.

The original analysis was performed in a local rotating reference frame (the original intention being to examine the possibility

of such instabilities in the interiors of rotating stars). The equations of motion considered in that work are akin to the local shearing sheet approximation familiar to accretion disc theory (Goldreich & Lynden-Bell 1965). Since this is our concern here we shall use that as our starting model set. The equations for axisymmetric dynamics in that environment are therefore

$$\begin{split} \frac{du}{dt} - 2\Omega_0 v &= -c_s^2 \frac{\partial \Pi}{\partial x} - \frac{\partial c_s^2}{\partial x} + 3\Omega_0^2 x, \\ \frac{dv}{dt} + 2\Omega_0 u &= 0, \\ \frac{dw}{dt} &= -c_s^2 \frac{\partial \Pi}{\partial z} - g, \\ \frac{d\Pi}{dt} + \frac{\partial u}{\partial x} + \frac{\partial w}{\partial z} &= 0, \end{split} \tag{A1}$$

where the expressions appearing are consistent with those developed in the body of the text recalling especially that $\Pi=\ln\rho$ and $\Omega_0=$ constant (see Sect. 6). The remaining expressions are defined again for convenience below. The only difference is that we use lower case letters for the radial, aziumthal and vertical velocities (i.e. u,v,w) in order to distinguish them from the ones used to describe dynamics in a cylindrical geometry examined in the main text of our study. Typically speaking, the vertical component of gravity is vertically varying and is given by $g=\Omega_0^2z$ - but for this analysis it is treated as a constant.

As done in GS67, one can do a point expansion (see the discussion of GS67 right prior to eq. 17 of that work) around any nominal level $z = z_0$. We start by considering the mean states which we represent with overbars. Thus,

$$-2\Omega_0 \overline{V} = -c_s^2 \frac{\partial \overline{\Pi}}{\partial x} - \frac{\partial c_s^2}{\partial x},$$
$$0 = -c_s^2 \frac{\partial \overline{\Pi}}{\partial z} - g.$$

Note that the mean azimuthal flow state \bar{v} has been decomposed into a keplerian piece (the term $-(3/2)\Omega_0 x$) plus a deviation about that state \bar{V} , i.e. $\bar{v} = -q\Omega_0 x + \bar{V}$. As before, c_s^2 is the sound speed (implicitly a function of x because of the radial dependence of the vertically isothermal temperature profile). In steady state we find that

$$\frac{\partial \overline{\Pi}}{\partial z} = -\frac{g}{c^2},$$

and, most importantly, the mean gradient of the azimuthal flow is

$$\bar{V}_z \equiv \frac{\partial \bar{V}}{\partial z} = \frac{g}{2\Omega_0} \frac{\partial \ln c_s^2}{\partial x}.$$
 (A2)

Perturbations of Π and all other variables around their reference means states are introduced with prime notation, e.g. $\Pi \to \bar{\Pi} + \Pi'$, etc. We assume an isothermal equation of state for the perturbations as well. Linearised perturbations of the equations of motion reveal

$$\frac{\partial u'}{\partial t} - 2\Omega_0 v' = -c_s^2 \frac{\partial \Pi'}{\partial x}$$

$$\frac{\partial v'}{\partial t} + \Omega_0 \left(1/2 + \overline{V}_x \right) u' + \overline{V}_z w' = 0$$

$$\frac{\partial w'}{\partial t} = -c_s^2 \frac{\partial \Pi'}{\partial z}$$

$$\frac{\partial \Pi'}{\partial t} + u' \frac{\partial \overline{\Pi}}{\partial x} + w' \frac{\partial \overline{\Pi}}{\partial z} + \frac{\partial u'}{\partial x} + \frac{\partial w'}{\partial z} = 0.$$
(A3)

Note we have utilised the shortened notation $\overline{V}_x \equiv \partial \overline{V}/\partial x$. To emphasize: the analysis we carry out here pointedly departs from that

done in GS67 in two respects: (i) we assume an isothermal equation of state for the disturbances and (ii) we allow for compressibility (cf. eq. 29 of GS67). Since g is constant, the above equations are easily combined into a single one for Π' yielding,

$$\begin{split} &\frac{\partial^{4}\Pi'}{\partial t^{4}} - \left[\left(\frac{\partial \overline{\Pi}}{\partial z} + \frac{\partial}{\partial z} \right) c_{s}^{2} \frac{\partial}{\partial z} + \left(\frac{\partial \overline{\Pi}}{\partial x} + \frac{\partial}{\partial x} \right) c_{s}^{2} \frac{\partial}{\partial z} - \kappa_{0}^{2} \right] \frac{\partial^{2}\Pi'}{\partial t^{2}} \\ &+ \left[2\Omega_{0} \overline{V}_{z} \left(\frac{\partial \overline{\Pi}}{\partial x} + \frac{\partial}{\partial x} \right) c^{2} - \kappa_{0}^{2} \left(\frac{\partial \overline{\Pi}}{\partial z} + \frac{\partial}{\partial z} \right) c_{s}^{2} \right] \frac{\partial \Pi'}{\partial z} = 0 \end{split} \tag{A4}$$

where the epicyclic frequency is represented by κ_0 and is related to the steady state quantities by

$$\kappa_0^2 = 2\Omega_0^2 (1/2 + \bar{V}_x).$$

Paraphrasing directly from GS67 (right prior to eq. 17 of that work): The next step is to expand the unperturbed variables and their derivatives in Taylor series about some point $x = x_0$ and $z = z_0$. The latter restriction is not as arbitrary as it might seem - it just makes the calculation more transparent. Discarding terms of order $(x - x_0)/x_0$ and $(z - z_0)/z_0$ the perturbation variables may be expanded in plane waves of the form $\sim e^{i(\omega t + k_x x + k_z z)}$, revealing the dispersion relationship

$$\omega^4 - \left[c_0^2(k_x^2 + k_z^2) + igk_z + \kappa_0^2\right]\omega^2 - 2\Omega_0\bar{V}_z c_0^2 k_x k_z + \kappa_0^2(c_0^2 k_z^2 + ik_z g) = 0,$$

in which c_0^2 is the sounds speed at the point in question and where $\kappa_0 \to \Omega_0$. As is standard for problems of atmospheres, we can recast the vertical wave dependence to have a complex character (indicating a basic wavey pattern) by defining $k_z \to k_z - ig/(2c_0^2)$ which renders the dispersion relation into the form

$$\omega^4 - \left[c_0^2(k_x^2 + k_z^2) + \kappa_0^2 + N_0^2\right]\omega^2 - 2\Omega_0\bar{V}_z c_0^2 k_x k_z + \kappa_0^2(c_0^2 k_z^2 + N_0^2) = 0,$$
(A5)

where we have defined the Brunt-Vaisaila frequency

$$N_0^2 = \frac{g^2}{4c_0^2}$$
.

Solutions for ω are easy to obtain and write down. It is more instructive, however, to assess the stability characteristics straight from an analysis of (A5) itself.

The classical GSF instability is one in which the modes pass through zero frequency before becoming unstable and they describe the influence that the vertical shear gradient has upon *inertial modes*. In our dispersion relation this amounts to the instability condition

$$-2\Omega_0 \bar{V}_z c_0^2 k_x k_z + \kappa_0^2 (c_0^2 k_z^2 + N_0^2) < 0.$$
 (A6)

When $c_0^2 k_z^2 \gg N_0^2$ the condition reduces to

$$-2\Omega_0 \bar{V}_z + \kappa_0^2 \frac{k_z}{k} < 0,$$

which is essentially the first term appearing in eq. 33 of GS67 (misprinted). Also, this condition is identical to that found in Urpin (2003), eq. 20. These latter correspondences follow from realizing that

$$\bar{V}_z \leftrightarrow \frac{\partial \Omega}{\partial z}, \qquad \frac{\kappa_0^2}{2\Omega_0} \leftrightarrow \frac{1}{R_0^2} \left(\frac{\partial R^2 \Omega}{\partial R}\right)_{R=R_0}$$

and, thus, recovering the classical Goldreich-Schubert condition. The dispersion relation (A5) has the general form

$$\omega^4 - B\omega^2 + C = 0$$

where B and C are obviously identified with the terms in (A5).

This equation has imaginary solutions for ω if (i) C < 0 with B > 0 or (ii) $B^2 - 4C < 0$. The GSF criterion (A6) is essentially the condition that C < 0. Condition (ii) is for acoustic-inertial modes to be unstable. This amounts to

$$\left[c_0^2(k_x^2 + k_z^2) + \kappa_0^2 + N_0^2\right]^2 - 4\left[-2\Omega_0\bar{V}_zc_0^2k_xk_z + \kappa_0^2(c_0^2k_z^2 + N_0^2)\right] < 0.$$
(A7)

A detailed examination of the behaviour of this condition shows that it does not occur for reasonable values of the parameters leading us to conclude that the acoustic modes (per se) do not become unstable as well.